SOURCE DATA   TRANSPARENT PROCESS   OPEN ACCESS

Mechanistic insights into enhancement or inhibition of phase separation by different polyubiquitin chains

Thuy P Dao[1,†], Yiran Yang[2,†], Maria F Presti[3] (ID), Michael S Cosgrove[3] (ID), Jesse B Hopkins[4] (ID), Weikang Ma[4] (ID), Stewart N Loh[3] & Carlos A Castañeda[1,5,*] (ID)

Abstract

Ubiquitin-binding shuttle UBQLN2 mediates crosstalk between proteasomal degradation and autophagy, likely via interactions with K48- and K63-linked polyubiquitin chains, respectively. UBQLN2 comprises self-associating regions that drive its homotypic liquid–liquid phase separation (LLPS). Specific interactions between one of these regions and ubiquitin inhibit UBQLN2 LLPS. Here, we show that, unlike ubiquitin, the effects of multivalent polyubiquitin chains on UBQLN2 LLPS are highly dependent on chain types. Specifically, K11-Ub4 and K48-Ub4 chains generally inhibit UBQLN2 LLPS, whereas K63-Ub4, M1-Ub4 chains, and a designed tetrameric ubiquitin construct significantly enhance LLPS. We demonstrate that these opposing effects stem from differences in chain conformations but not in affinities between chains and UBQLN2. Chains with extended conformations and increased accessibility to the ubiquitin-binding surface promote UBQLN2 LLPS by enabling a switch between homotypic to partially heterotypic LLPS that is driven by both UBQLN2 self-interactions and interactions between multiple UBQLN2 units with each polyubiquitin chain. Our study provides mechanistic insights into how the structural and conformational properties of polyubiquitin chains contribute to heterotypic LLPS with ubiquitin-binding shuttles and adaptors.

Introduction

Protein quality control (PQC) mechanisms, which enable cells to combat aberrant proteins, is essential for cellular functions and viability (Vendruscolo, 2012; Dikic, 2017). Several distinct but connected pathways, such as proteasomal degradation, endoplasmic reticulum-associated protein degradation, and autophagy, exist to ensure proper PQC. In most cases, ubiquitination of substrate proteins is the common signal for these different pathways, and numerous other processes, such as DNA damage response, cargo transport, and cell-cycle control (Komander & Rape, 2012). This wide range of cellular responses to ubiquitination stems from the ability of ubiquitin (Ub) to form polyubiquitin (polyUb) chains with different lengths and linkages. The two most abundant and well-studied polyUb chain types are K48- and K63-linked chains that generally signal for proteasomal degradation and autophagy, respectively. Other chains, such as K11- and M1-linked chains, are involved in degradative and nonproteolytic pathways, respectively (Akutsu et al, 2016). It is hypothesized that polyUb chains elicit different biological signaling outcomes based on differences in their conformational properties and how each chain type interacts with Ub-binding receptors, such as shuttle proteins (Komander & Rape, 2012). Different shuttle proteins can recognize specific chains and transport modified substrates to distinct pathways (Komander & Rape, 2012; Zientara-Rytter & Subramani, 2019). Some shuttle proteins, such as autophagy receptor NBR1 and proteasomal shuttle protein hHR23B, are mostly pathway-specific. Others, such as UBQLN2 and p62, are involved in multiple pathways (Zientara-Rytter & Subramani, 2019). How shuttle proteins choose a specific pathway upon binding to ubiquitinated substrates, possibly through changes in conformations or oligomeric states, is of great interest (Lu et al, 2017).

PQC impairment due to aging, prolonged stress, or mutations can lead to protein-containing inclusions characteristic of neurodegenerative diseases, such as amyotrophic lateral sclerosis (ALS),

1 Departments of Biology and Chemistry, Syracuse University, Syracuse, NY, USA
2 Department of Chemistry, Syracuse University, Syracuse, NY, USA
3 Department of Biochemistry and Molecular Biology, SUNY Upstate Medical University, Syracuse, NY, USA
4 The Biophysics Collaborative Access Team (BioCAT), Department of Biological Sciences, Illinois Institute of Technology, Chicago, IL, USA
5 Interdisciplinary Neuroscience Program, Syracuse University, Syracuse, NY, USA
*Corresponding author. Tel: +1 315 443 3673; E-mail: cacastan@syr.edu
†These authors contributed equally to this work

Parkinson's, and Alzheimer's diseases (Hipp *et al*, 2014; Labbadia & Morimoto, 2015). These inclusions often comprise Ub, polyUb chains, Ub-binding shuttle proteins, and other PQC proteins (Lowe *et al*, 1988; Manetto *et al*, 1988; Riley *et al*, 2010; Morimoto *et al*, 2015). Many of these proteins are also part of membraneless compartments, such as stress granules and PQC compartments that sequester aberrant proteins in preparation for clearance in healthy eukaryotic cells (Sontag *et al*, 2017). Dysregulation of membrane-less compartments can lead to disease-linked inclusions (Molliex *et al*, 2015; Patel *et al*, 2015; Nedelsky & Taylor, 2019; Ryan & Fawzi, 2019). Liquid–liquid phase separation (LLPS) of a few key scaffolding proteins drive the formation of membraneless compartments whereas interacting partners of scaffolding proteins can modulate the properties of these compartments (Guillén-Boixet *et al*, 2020; Sanders *et al*, 2020; Yang *et al*, 2020; Yasuda *et al*, 2020). Therefore, knowledge of how binding partners affect phase-separating scaffolds is essential for understanding the regulation of PQC mechanisms.

We recently showed that the Ub-binding shuttle protein UBQLN2 phase separates under physiological conditions, but specific interactions with Ub, K48-linked Ub2, and Ub4 disrupt UBQLN2 LLPS (Dao *et al*, 2018). Following the polyphasic linkage formalism put forth by Wyman and Gill, UBQLN2 is considered a scaffold that drives condensate formation and Ub/K48 polyUb chains are ligands that can modulate LLPS (Wyman & Gill, 1980). Ligands can either enhance or inhibit LLPS, depending on their multivalency (in this case, the number of Ub units in a chain) and binding preferences for the scaffold in the dense and dilute phases (Ruff *et al*, 2021a). Unlike UBQLN2, proteasomal shuttle protein hHR23B and autophagy receptor p62 require longer K48- and K63-linked polyUb chains, respectively, to phase separate and carry out their functions (Sun *et al*, 2018; Yasuda *et al*, 2020). Interestingly, UBQLN1, which is a close homolog of UBQLN2 and is involved in both autophagy and proteasomal degradation, might bind preferentially to K63- over K48-linked chains (Harman & Monteiro, 2019). Therefore, we hypothesized, and showed in this work, that different polyUb chain types elicit distinct effects on UBQLN2 LLPS. By studying the interactions between UBQLN2 and various naturally occurring and designed polyUb chains, we determined the molecular mechanisms underlying these drastically different effects on UBQLN2 LLPS. Our results offer insights into how polyUb chains of distinct linkages drive ligand-induced phase transitions, and how modulation of UBQLN2 LLPS may steer UBQLN2 involvement into various PQC pathways.

Results

PolyUb chains with distinct linkage types and lengths differentially affect UBQLN2 LLPS

To determine whether various polyUb chains impact UBQLN2 LLPS behavior differently, we initially focused on enzymatically synthesized K48 and K63 chains of two, three, and four Ub units (Appendix Fig S1A). These two chains are the most abundant in cells, signal for different cellular events, exhibit distinct solution conformations, and selectively drive LLPS of other Ub-binding shuttle proteins (Ye *et al*, 2012; Castañeda *et al*, 2016a; Sun *et al*, 2018; Dao & Castañeda, 2020; Yasuda *et al*, 2020).

We first screened for the effects of polyUb chains on full-length (FL) UBQLN2 LLPS by imaging UBQLN2 droplets that settle onto the coverslip at different Ub:UBQLN2 ratios (Fig 1A). When LLPS was first induced, droplets from different solutions appeared to be similar in size. However, samples with increased LLPS contained more droplets that subsequently fuse and settle as large droplets on the coverslip. Consistent with our previous data, increasing amounts of Ub disassembled UBQLN2 droplets (Dao *et al*, 2018, 2019). Using nuclear magnetic resonance (NMR) spectroscopy, we confirmed that Ub binds only to the Ub-associated (UBA) domain in UBQLN2 with a K_d of 3 μM (similar to K_d for Ub binding to UBQLN2 450–624; Dao *et al*, 2018); only amide peaks of UBA residues shifted in the presence of Ub (Appendix Fig S1B). As Ub binds to the same UBA sites that are important for UBQLN2 LLPS (Appendix Fig S1C; Dao *et al*, 2018), we classified Ub as a monovalent ligand that interacts with UBA stickers and destabilizes LLPS (Ruff *et al*, 2021a).

In contrast to Ub, K48- and K63-Ub2, Ub3, and Ub4 chains can be considered divalent, trivalent, and tetravalent ligands that bind to UBQLN2. We observed several trends when mixing these multivalent ligands with UBQLN2: (i) Droplets were observed at increasingly higher Ub:UBQLN2 ratios as chain length/multivalency increased, regardless of linkage type. (ii) Longer K63 chains significantly promoted UBQLN2 LLPS at lower Ub:UBQLN2 ratios. (iii) All chains inhibited LLPS at higher ratios (Fig 1A).

K63-Ub4 promotes reentrant phase behavior of UBQLN2

To quantitatively describe the effects of polyUb on UBQLN2 LLPS, we ran turbidity experiments that monitored the change in A_{600} values as a function of temperature at different Ub:UBQLN2 ratios. The UBA domain of UBQLN2 was folded and able to interact with Ub at the temperature range used in our assays (Appendix Fig S2A). We previously showed that high and low A_{600} values correlate with droplet formation and clearance, respectively, and that UBQLN2 phase separates with increasing temperature (Dao *et al*, 2018). Increasing amounts of Ub and K48-Ub2 reduced and eventually eliminated UBQLN2 LLPS (Fig 1B; Dao *et al*, 2018). The turbidity plots for K63-Ub2 addition to UBQLN2 were nearly identical to those of K48-Ub2 and Ub, suggesting that lysine linkage does not matter at the Ub2 level.

The addition of Ub3 and Ub4 chains of different linkages led to distinct turbidity plots (Fig 1B; Appendix Fig S2B), consistent with microscopy data (Fig 1A). Strikingly, K63-Ub4 visibly promoted and inhibited LLPS, depending on Ub:UBQLN2 ratio, reminiscent of reentrant phase behavior seen for protein-nucleic acid and protein–protein coacervates that form via heterotypic interactions (Banerjee *et al*, 2017; Alshareedah *et al*, 2019; Choi *et al*, 2019; Dignon *et al*, 2020; Xu *et al*, 2020; Feric *et al*, 2021). Low K63-Ub3/Ub4:UBQLN2 ratios significantly promoted LLPS, driving UBQLN2 droplet assembly at lower temperatures than in the absence of K63-Ub3/Ub4. As these ratios were further increased, LLPS was inhibited. We hypothesized that K63-Ub4 promotes LLPS by acting as an emergent scaffold onto which multiple UBQLN2 molecules bind. These heterotypic interactions provide additional multivalency to further promote LLPS. However, as Ub4 concentrations increase, not enough UBQLN2 molecules exist to bind Ub4 simultaneously, hence diluting the LLPS-driving UBQLN2-UBQLN2 interactions and leading to inhibition of LLPS (Banerjee *et al*, 2017; Choi *et al*, 2019;

Dao & Castañeda, 2020; Ruff *et al*, 2021b). Conversely, low K48-Ub3/Ub4:UBQLN2 ratios only slightly enhanced LLPS (Appendix Fig S2B). Increasing the addition of K48-Ub3/Ub4 inhibited LLPS at much lower Ub:UBQLN2 ratios than for K63-Ub3/Ub4.

To quantitatively compare the effects of polyUb chains on UBQLN2 LLPS, we obtained temperature-composition phase diagrams for different Ub:UBQLN2 ratios at multiple UBQLN2

concentrations (Fig 1C). We determined T_{cp}(infl), the cloud point temperature at the inflection point of the transition (Yang *et al*, 2019). We used T_{cp} at different Ub:UBQLN2 ratios to map out the coexistence curve, above which the protein solution is phase-separated. For Ub and Ub2, we observed a linear increase in T_{cp} as Ub:UBQLN2 ratio increased, consistent with Ub and Ub2 being low-valency ligands that interact with UBQLN2 UBA "stickers" (UBQLN2
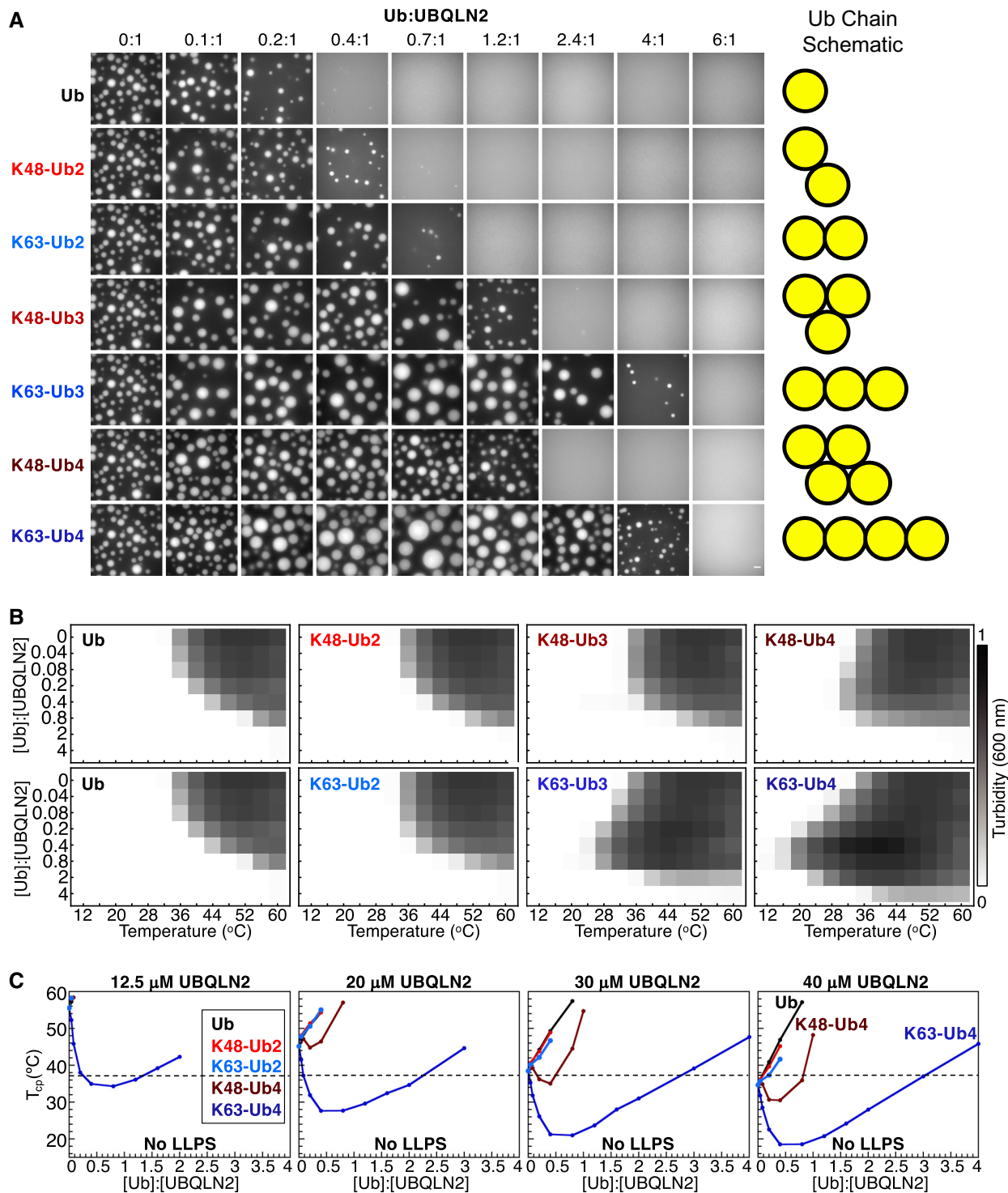

Figure 1.

residues that are important for self-association and LLPS) to drive droplet disassembly (Dao *et al*, 2018). In contrast, we observed a substantial decrease in T_{cp} at low K63-Ub4:UBQLN2 ratios, indicating a greater regime of the phase diagram over which UBQLN2 is phase-separated. This effect was clearest at the lowest concentration tested (12.5 μM), which approaches the physiological UBQLN2 concentration (1–2 μM) (Dao *et al*, 2018). At 37°C, 12.5 μM UBQLN2 did not phase separate by itself or with Ub, K48-Ub2, K63-Ub2, and K48-Ub4, but readily phase-separated with K63-Ub4 between Ub:UBQLN2 ratios of 0.3:1 (~1 μM K63-Ub4) and 1.3:1 (4 μM K63-Ub4). Our data illustrate a transition from UBQLN2 LLPS driven by homotypic interactions to a system where LLPS is driven, at least partially, by heterotypic interactions between UBQLN2 and K63-Ub4 (Dao & Castañeda, 2020). Therefore, polyUb chains of different linkages can substantially alter the driving forces of phase-separating systems.

NMR and fluorescence anisotropy titrations reveal differences in how K48- and K63-Ub4 interact with UBQLN2

To examine the molecular origins of the differential effects of K48- or K63-Ub4 on UBQLN2 LLPS, we used NMR to map the interactions between Ub4 and UBQLN2. First, we looked at FL UBQLN2 in the presence of Ub4, but the UBA resonances were severely attenuated, precluding quantitative NMR studies (Appendix Fig S3A). To circumvent this issue, we used UBQLN2 450–624, a C-terminal construct that exhibits LLPS behavior similar to FL UBQLN2 and is amenable to NMR studies (Dao *et al*, 2018, 2019). We obtained temperature-composition phase diagrams using UBQLN2 450–624 and different amounts of K48- or K63-Ub4. Our phase diagrams showed that the two Ub4s alter LLPS of 450–624 in a similar manner as for FL UBQLN2 (Appendix Fig S3B). Therefore, for subsequent NMR experiments, we collected data using UBQLN2 450–624 under non-phase-separating conditions.

Upon titration of K48- or K63-Ub4 into ^{15}N-labeled UBQLN2 450–624, we observed a broadening of UBA peaks, likely due to the large size of the Ub4:UBQLN2 450–624 complex (> 35 kDa Ub4 + 1-4X 17 kDa UBQLN2 450–624). Despite this, we could follow the resonances and observe chemical shift perturbations (CSPs) mainly for UBA residues (Fig 2A), indicating that Ub units in the chains bind primarily to UBA and in a manner like monoUb. However, we also observed CSPs (Fig 2A) and reduced peak intensity (Fig 2B) for residues 555–570, more so with K48-Ub4 than K63-Ub4, which adopt compact and extended solution conformations in the unbound state, respectively (Tenno *et al*, 2004). We recapitulated the same trends with UBQLN2 487–624 (Fig 2C). Resonances in UBQLN2 487–624 exhibit better NMR signal-to-noise quality since this construct does

not oligomerize, undergo LLPS, or exhibit backbone dynamics on a slow millisecond timescale (Dao *et al*, 2018). Residues 555–570 were not perturbed in the presence of monoUb (Dao *et al*, 2018). Furthermore, we did not observe CSPs outside of the UBA domain in a UBQLN2 450–624 construct lacking residues 551–569 (Fig 2D). Residues 555–570, but not the surrounding regions, exhibit slight helical propensity (Dao *et al*, 2018). Together, these data suggest that the transiently helical 555–570 region either specifically interacts with K48-Ub4 or is sterically affected when the compact K48-Ub4 binds to UBA. Since the 555–570 region is a "sticker" that mediates UBQLN2 LLPS (Dao *et al*, 2018), we speculated that K48-Ub4 may inhibit UBQLN2 LLPS by preventing both UBA and 555–570 stickers from contributing to LLPS.

To determine the binding affinities between K48- or K63-Ub4 and UBQLN2, we collected residue-specific titration curves for resonances in UBQLN2 450–624 with the two Ub4s (Fig 2E). The curves for UBQLN2 amide resonances were sigmoidal, especially for the titration with K48-Ub4, and resonances exhibited extensive line broadening. These conditions preclude us from considering CSPs as simple weighted averages of free and bound species, as we are no longer under fast exchange conditions (Williamson, 2013). Instead, we used TITAN 2D lineshape analysis (Waudby *et al*, 2016), which accounts for both CSP and peak broadening during the titration, to obtain K_d values. Assuming single-site binding between UBQLN2 and each Ub unit in Ub4, we obtained binding affinities of 3 μM for both Ub and K63-Ub4, and a lower affinity of 25 μM for K48-Ub4 (Fig 2F; Appendix Figs S6A–F and Table S1). We corroborated our NMR measurements of K_d values using fluorescence anisotropy experiments. Anisotropy monitors how quickly the fluorophore tumbles and reorients in solution, which is influenced by the size and flexibility of the protein to which the fluorophore is attached (higher anisotropy indicates larger size and/or decreased flexibility). We observed increases in anisotropy on titrating K48-Ub4, K63-Ub4, and Ub into fluorescently-labeled UBQLN2 450–624 (Fig 2F and G). The fitted K_d values for UBQLN2 with Ub, K48-Ub4, and K63-Ub4 were 3.4, 0.4, and 2.3 μM, respectively (Fig 2F; Appendix Table S1). Interestingly, like NMR, anisotropy reported very similar K_d values for binding between UBQLN2 and Ub or K63-Ub4 but not K48-Ub4.

To further investigate the differences in K_d values for K48-Ub4 between NMR and anisotropy, we carried out the reciprocal anisotropy experiments in which we titrated UBQLN2 450–624 into K48-Ub4 or K63-Ub4 containing a fluorescently-labeled Ub unit (see Methods). There was minimal change in anisotropy for K63-Ub4 with increasing amounts of UBQLN2, indicating minimal differences in how the complex tumbled compared with how the fluorescently-labeled Ub unit in K63-Ub4 tumbled (Fig 2H). In contrast, anisotropy significantly decreased upon K48-Ub4 binding to UBQLN2.
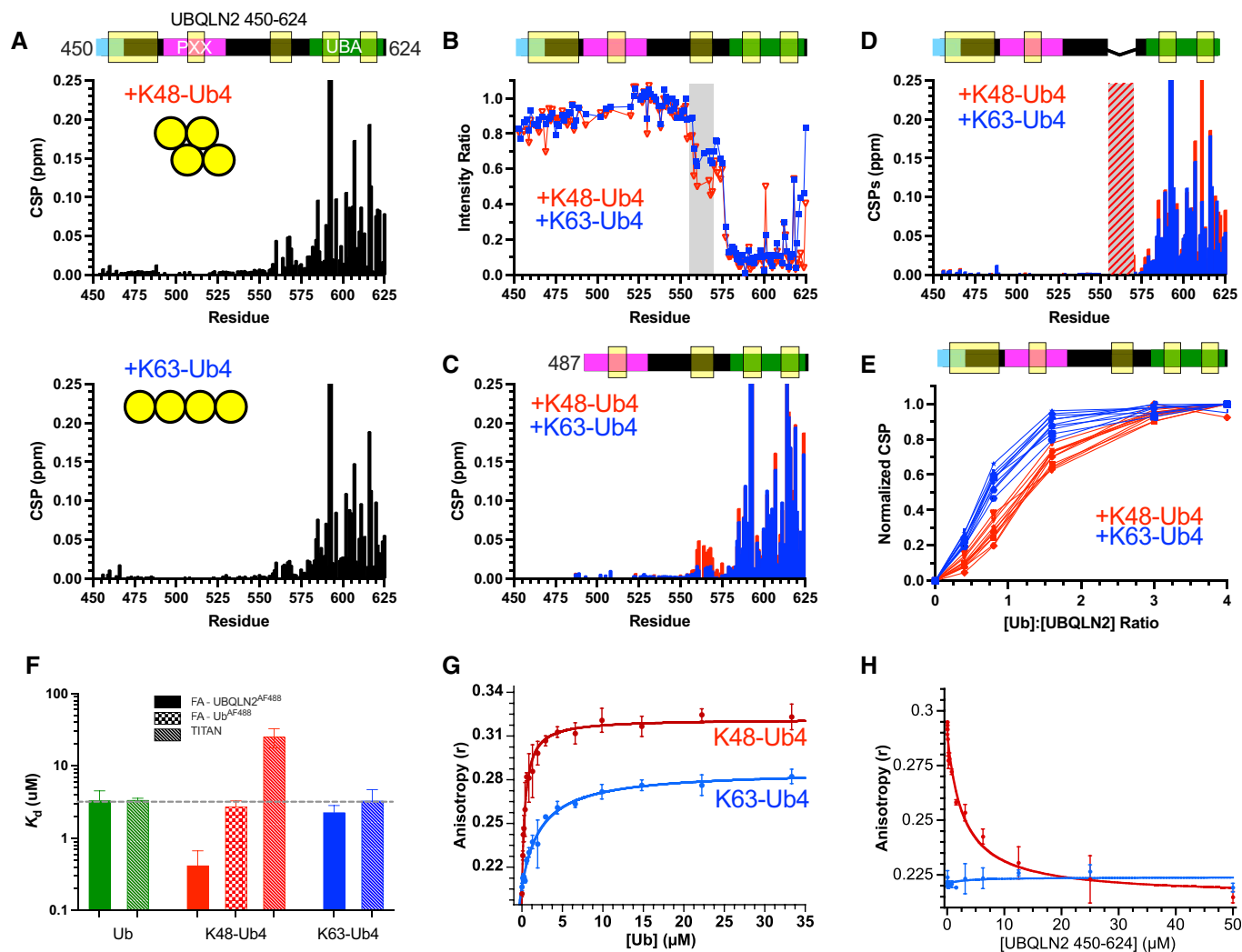
Figure 2. K48- and K63-Ub4 bind differently to UBQLN2 450–624.

A CSP for UBQLN2 450–624 residues at 1:1 ratio with Ub4. The highlighted regions in the domain map are important for the homotypic interactions that drive UBQLN2 LLPS (Dao et al, 2018).

B Amide peak intensities between the unbound and Ub4-bound forms of UBQLN2 450–624 with the 555–570 region highlighted in gray.

C CSPs for residues in UBQLN2 487–624 at 1:1 ratio with Ub4.

D CSPs for residues in UBQLN2 450–624 lacking residues 551–569 (red/gray region) at 1:1 ratio with Ub4.

E Normalized titration curves of 11 amide resonances for UBQLN2 450–624.

F Comparison of binding affinity (K_d) measurements obtained from NMR and fluorescence anisotropy. Error bars for the FA numbers represent the standard deviation over three biological trials and for the TITAN numbers are from jackknife analysis. For visual comparison, gray dashed line is K_d of Ub binding to UBQLN2 450–624 as determined from NMR and FA experiments (green bars).

G Fluorescence anisotropy values for fluorescently-labeled UBQLN2 450–624 in the presence of increasing K48- or K63-Ub4. Error bars represent the standard deviation over three biological trials.

H Fluorescence anisotropy values for fluorescently-labeled K48- or K63-Ub4 in the presence of increasing UBQLN2 450–624. Error bars represent the standard deviation over three biological trials.

Source data are available online for this figure.

This decrease in anisotropy is atypical and indicates that the binding of UBQLN2 to K48-Ub4 caused the latter to become more flexible despite the increased mass of the complex (Fig 2H). Titrating UBQLN2 into K48-Ub4 with a labeled Ub unit yielded a K_d of 2.7 μM, similar to the K_d values for UBQLN2 and K63-Ub4 by NMR and anisotropy. We hypothesized that the conflicting binding data from NMR and anisotropy stemmed from differences in conformations of K48-Ub4 and K63-Ub4.

The Ub-Ub interface in K48-Ub4 "opens" to accommodate UBQLN2 binding

K48- and K63-Ub4 are known to adopt compact and extended conformations, respectively, with the latter containing Ub units in a beads-on-a-string arrangement (Fig 3A). Indeed, small-angle x-ray scattering (SAXS) (Appendix Table S2) showed that unbound K48-Ub4 is compact (R_g = 25.67 ± 0.05 Å), whereas K63-Ub4 is
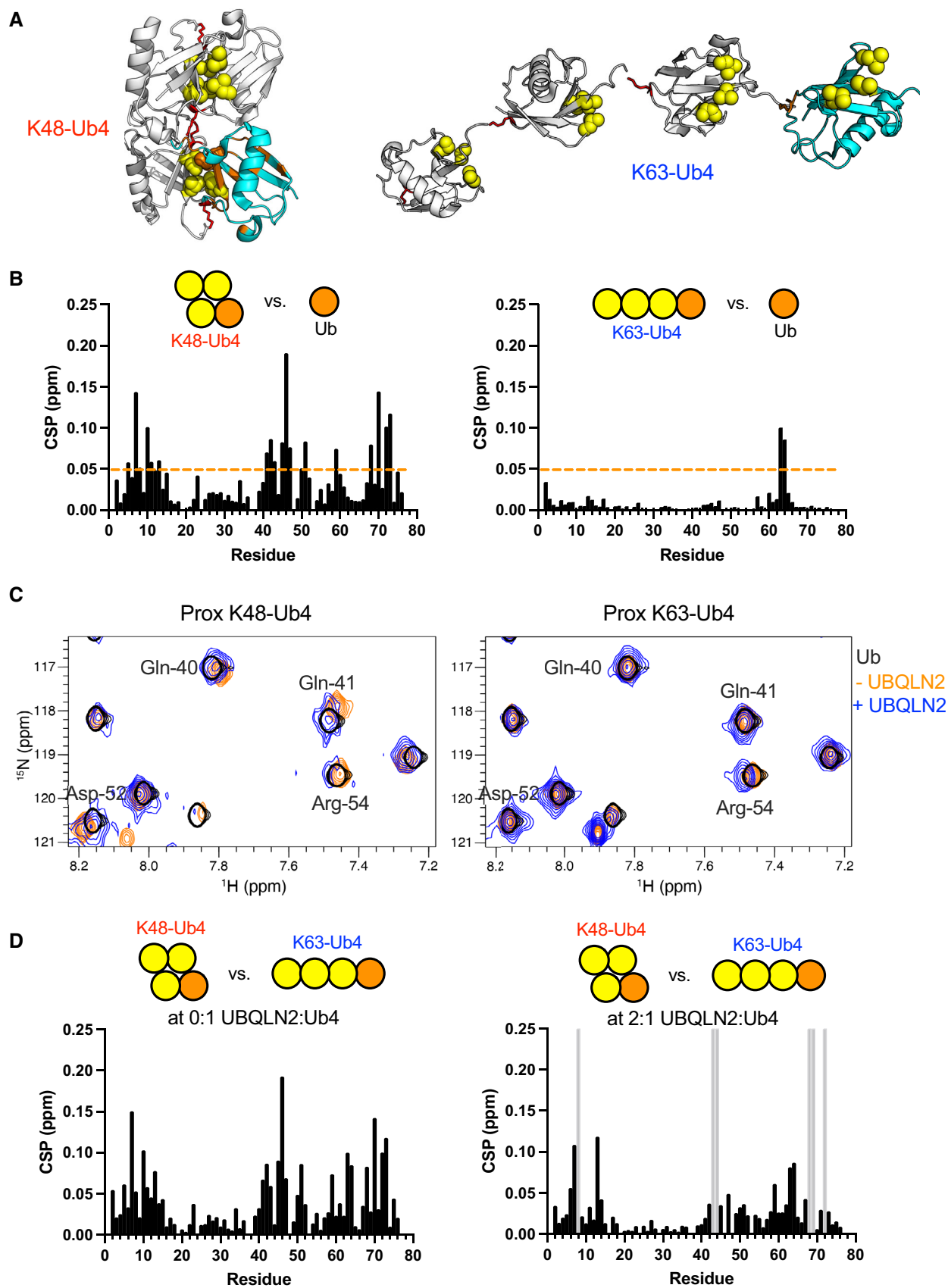
Figure 3.

Figure 3. The Ub–Ub interface in K48-Ub4 opens to bind to UBQLN2.

A   Representative structures of K48-Ub4 (PDB ID 2O6V) and K63-Ub4 (PDB ID 3HM3). The cyan proximal Ub unit was selectively ^{15}N-labeled for NMR-binding experiments. Yellow spheres represent hydrophobic patch residues L8, I44, and V70. Red sticks indicate K48 or K63 linkage. CSPs > 0.05 ppm for proximal Ub resonances vs. monoUb positions (in the absence of UBQLN2) are color-coded orange.

B   Proximal Ub resonances in Ub4 were compared with monoUb, as noted in the schematic diagram. CSPs > 0.05 ppm (orange dashed line) are mapped onto the proximal Ub unit of Ub4 in panel A.

C ^{15}N-^{1}H SOFAST-HMQC NMR spectra of proximal Ub of K48-Ub4 or K63-Ub4 at 50 μM in the absence and presence of UBQLN2 450–624 at a 2:1 UBQLN2:Ub4 ratio. Unbound monoUb spectrum (black) is overlaid for comparison. NMR spectra collected and processed under identical conditions.

D   CSPs of the same proximal Ub resonances in K63-Ub4 vs. K48-Ub4. Gray bars indicate K48-Ub4 resonances that were too weak to be detected.

Source data are available online for this figure.

extended ($R_g = 32.33 \pm 0.09$ Å), consistent with prior structural studies (Varadan *et al*, 2002; Tenno *et al*, 2004). Sedimentation velocity analytical ultracentrifugation (SV-AUC) data support these conclusions, as K48-Ub4 has a higher sedimentation coefficient and lower frictional ratio than K63-Ub4 (Appendix Fig S4 and Table S3). We also observed higher anisotropy for fluorescently-labeled UBQLN2 upon titration of K48-Ub4 compared with K63-Ub4 (Fig 2 G). These data suggest that, as the limiting reagent, only one UBQLN2 would bind to each K48-Ub4, which remains compact, and therefore, high anisotropy is observed for the large UBQLN2/K48-Ub4 complex. In contrast, when UBQLN2 is bound to an individual Ub bead on a K63-Ub4 string, the anisotropy for the UBQLN2/K63-Ub4 complex is not as high due to the smaller size of the tumbling unit. With the reciprocal titration where K48-Ub4 is the limiting reagent, anisotropy significantly decreased, suggesting that K48-Ub4 must open to accommodate simultaneous binding of multiple UBQLN2, leading to the fluorescently-labeled Ub tumbling more independently as a smaller unit from the rest of the Ub4 chain.

To test our hypothesis that K48-Ub4 changes from a compact to a more extended conformation upon interacting with UBQLN2 450–624, we performed NMR titration of UBQLN2 450–624 into either K48 or K63-Ub4 with ^{15}N-labeled proximal Ub (Fig 3A). First, we compared the HSQC spectrum of each proximal Ub unit to monoUb (in the absence of UBQLN2) and found significant CSPs for resonances in the proximal Ub of K48-Ub4 but not K63-Ub4, indicative of Ub-Ub interactions among K48-Ub4 subunits (Fig 3B). The large CSPs map to the UBQLN2-binding hydrophobic patch of Ub (L8, I44, V70) and surrounding residues, consistent with known structures of K48-Ub4 (Fig 3A; Eddins *et al*, 2007). Together with SAXS and AUC data (Appendix Fig S4A–C and Tables S2 and S3), these data suggested that the K48-Ub4 is compact in solution and that the Ub hydrophobic patches are not immediately available to bind ligands.

Upon titration of UBQLN2 450–624, we observed that several resonances near the Ub-Ub interface (residues 10, 39, 40, 41, 51, 52, 73, 75) in the ^{15}N-labeled proximal Ub of K48-Ub4 converged to the locations of the same resonances in the unbound monoUb (Fig 3C), indicating that these resonances in proximal Ub of K48-Ub4, as UBQLN2 was titrated, were in similar chemical environments as free monoUb. In contrast, the same resonances in proximal Ub of K63-Ub4, in which no Ub units are in close contact with one another, did not move significantly with the initial addition of UBQLN2 (Fig 3C). In other words, the hydrophobic patch of the proximal Ub of K48-Ub4 exhibited different chemical environments than that of Ub and the proximal Ub of K63-Ub4 in the absence of UBQLN2 but was in similar local environments in the presence of UBQLN2 (Fig 3D). These data are consistent with our hypothesis that K48-Ub4 needs

to "open" to accommodate UBA binding, partially explaining the sigmoidal titration curves and the weaker NMR-derived apparent binding affinity for K48-Ub4 from the UBQLN2 450–624 side (see above and Appendix Table S1). Therefore, the Ub binding patch is readily accessible in K63-Ub4 but requires an additional conformational change in K48-Ub4 to interact with UBQLN2. These observations resulted from differences in chain conformations and not binding ability as SV-AUC experiments of K48- or K63-Ub4 in the presence of UBQLN2 487–624 at a 2:1 UBQLN2:Ub4 loading ratio showed complete binding between either chain with UBQLN2 (Appendix Fig S4A–C). The AUC data are consistent with a model where UBQLN2:K48-Ub4 complex is slightly more compact than the UBQLN2:K63-Ub4 complex (Appendix Table S3).

In summary, we suspect that K48-Ub4 does not readily promote UBQLN2 LLPS through heterotypic interactions because K48-Ub4 (1) interacts with the 555–570 "sticker" required for LLPS, (2) is compact in conformation, and (3) contains Ub hydrophobic patches that are not as readily accessible for UBQLN2 binding. In contrast, K63-Ub4 can act as a scaffold to promote LLPS since K63-Ub4 (1) minimally interacts with 555–570, (2) adopts an extended conformation, and (3) contains Ub hydrophobic patches that are readily accessible for UBQLN2 binding.

Effects of K11, M1-Ub4, and tetrameric HOTag6-G10-Ub on UBQLN2 binding

From the K48 and K63-Ub4 data, we hypothesized that differences in Ub4 conformation and Ub "sticker" accessibility are important determinants that drive differential effects on LLPS of UBQLN2. To test this hypothesis, we extended our study to examine how UBQLN2 interacts with other naturally occurring Ub4 chains, specifically K11 and M1 linkages, and a designed tetrameric HOTag6-G10-Ub (Fig 4A). K11-Ub4 exhibits a compact conformation similar to K48-Ub4, whereas M1-Ub4 is similar to K63-Ub4 in that it adopts an extended conformation and the Ub binding patches are readily accessible, as confirmed by SAXS (Fig 4B, Appendix Fig S5A). HOTag6-G10-Ub comprises HOTag6, which exists as a tetramer (Zhang *et al*, 2018), and tethered Ub, linked by 10 glycines, to form a tetrameric complex with high conformational flexibility between the Ub units (Fig 4B; Appendix Fig S5B–D). Therefore, these three constructs, together with K48- and K63-Ub4, form a library of Ub tetramers with varying conformations, flexibility, and hydrophobic patch accessibility to UBQLN2 (Fig 4A and B).

We used NMR spectroscopy to probe how these different polyUb chains interact with UBQLN2 450–624. As expected, we observed the largest CSPs for UBA resonances (Fig 4C). CSPs for K11-Ub4 were very similar to those for K48-Ub4, whereas CSPs for M1-Ub4
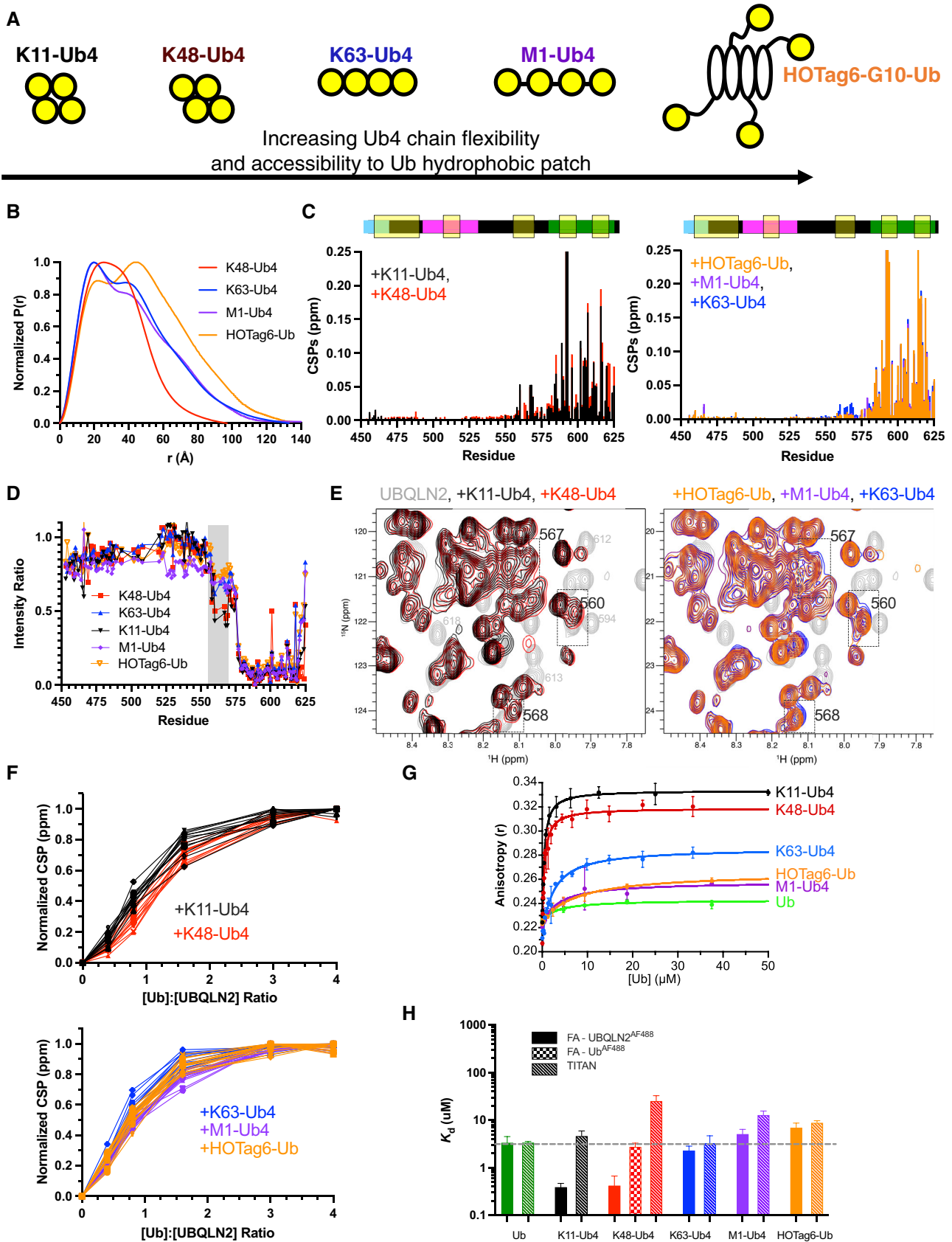
Figure 4.

Figure 4. Compact K11 and K48-Ub4 bind UBQLN2 differently than extended K63-Ub4, M1-Ub4, and HOTag6-G10-Ub.

A   Cartoons depicting a possible solution conformation for each of the Ub4 chains studied here.

B   Normalized pair distance distribution function $P(r)$ from SAXS data for four Ub4 chain types.

C   CSPs at 1:1 Ub4:UBQLN2 for all chain types but clustered into two categories for clarity.

D   Peak intensity comparison in the absence and presence of Ub4 at 1:1 Ub4:UBQLN2 with residues 555–570 highlighted in gray.

E   TROSY-HSQC spectra of UBQLN2 450–624 in the absence and presence of different Ub4 chains. Some of the peaks in the 555–570 region are more perturbed in the presence of K11-Ub4 and K48-Ub4 but not the other chains, whereas the UBA peaks (580–624) are equally perturbed in the presence of any of the chains.

F   Normalized titration curves of UBA resonances showing more pronounced sigmoidal behaviors upon titration of K48-Ub4 into UBQLN2 450–624 than upon titrations of K11-Ub4, K63-Ub4, M1-Ub4, and HOTag6-Ub.

G   Fluorescence anisotropy values for fluorescently-labeled UBQLN2 450–624 in the presence of increasing amounts of different Ub4 chains. Error bars represent the standard deviation over three biological trials.

H   Comparison of K_d values obtained from NMR and fluorescence anisotropy. Error bars for the FA numbers represent the standard deviation over three biological trials and for the TITAN numbers are from jackknife analysis. For visual comparison, gray dashed line is K_d of Ub binding to UBQLN2 450–624 as determined from NMR and FA experiments (green bars).

Source data are available online for this figure.

and HOTag6-G10-Ub were very similar to those for K63-Ub4. Amide resonances for residues 555–570 were more perturbed and peak intensities for residues 555–570 were more reduced in the presence of either compact K11- or K48-Ub4 chains, but not with the extended or more conformationally flexible M1-Ub4, K63-Ub4, or HOTag6-G10-Ub (Fig 4C–E).

Using NMR titration experiments and TITAN 2D lineshape analysis, we measured binding affinities between labeled UBQLN2 450–624 and these chain types (Fig 4F; Appendix Fig S6A–F). We obtained K_d values of 4.6, 12.8, and 8.8 μM for K11-Ub4, M1-Ub4, and HOTag6-G10-Ub, respectively (Fig 4H; Appendix Table S1). Unlike K48-Ub4 which is compact with occluded Ub hydrophobic patches, K11-Ub4 is compact with more exposed Ub hydrophobic patches (Appendix Fig S7A). Correspondingly, we observed that UBQLN2 NMR titration curves with K11-Ub4 barely exhibit sigmoidal behavior as K11-Ub4 might not need to open to accommodate UBQLN2 binding (unlike that of K48-Ub4). Despite K11-Ub4, M1-Ub4, and HOTag6-G10-Ub exhibiting different conformations in solution, their UBQLN2 binding surfaces are easily accessible (Appendix Fig S7B) and they exhibit similar K_d values with UBQLN2, indicative of minimal linkage preference between UBQLN2 and polyUb.

Fluorescence anisotropy experiments using fluorescently-labeled UBQLN2 450–624 revealed differences in the tumbling properties of the UBQLN2:Ub4 complexes (Fig 4G). With the addition of either K11- or K48-Ub4, the final anisotropy values for UBQLN2 were similarly high, suggesting that UBQLN2:K11-Ub4 and UBQLN2:K48-Ub4 complexes tumble slowly as large units. In contrast, the final anisotropy values for UBQLN2 were low with either HOTag6-G10-Ub or M1-Ub4, similar to the anisotropy value for UBQLN2 when saturated with Ub. Since both M1-Ub4 and HOTag6-G10-Ub comprise Ub units that are connected by highly flexible linkers (Fig 4A; Appendix Fig S7A), these data suggest that the Ub units in these two proteins move relatively independently. The anisotropy-derived K_d values for M1-Ub4 and HOTag6-G10-Ub were 5.1 and 7.0 μM, respectively, similar to those determined by NMR and for K63-Ub4 and Ub.

We note a tighter apparent anisotropy-derived K_d for K11-Ub4 of 0.39 μM, similar to that of K48-Ub4 (Fig 4H). Both K11- and K48-Ub4 adopt compact conformations but have differently accessible UBQLN2-binding sites, possibly leading to discrepancies between NMR- and anisotropy-derived K_d values. As UBQLN2 reagent is limiting (100 nM) under the anisotropy experimental conditions, the

UBQLN2:Ub4 complexes likely only have a single UBQLN2 bound. Given the compact arrangements of Ub units in both K11- and K48-Ub4, we speculate that when the UBQLN2 UBA domain binds to a Ub unit, a secondary interaction occurs between UBQLN2 and the rest of K11- or K48-Ub4. Indeed, we observed increased UBQLN2 CSPs for residues 555–570 adjacent to the UBA domain for both K11- and K48-Ub4 (Fig 4C), although these CSPs are significantly weaker than those observed for the UBA domain.

Together, our data suggest that all five chains have similar binding affinities to UBQLN2. However, because of their quaternary structures and solution conformations, we predicted that they may have different effects on UBQLN2 LLPS. Specifically, K11-Ub4 may affect UBQLN2 LLPS similarly to K48-Ub4 due to CSPs for residues 555–570 and K11-Ub4's compact conformation, whereas M1-Ub4 and HOTag6-G10-Ub may affect UBQLN2 LLPS similarly to K63-Ub4 due to similarities in binding affinity, extended conformation, and readily accessible Ub binding patches.

Extended and flexible, but not compact, polyUb chains promote UBQLN2 LLPS

Next, we performed microscopy and turbidity assay experiments to determine how K11-Ub4, M1-Ub4, and HOTag6-G10-Ub affect UBQLN2 LLPS. Microscopy showed that M1-Ub4 and HOTag6-G10-Ub stabilized UBQLN2 droplets over a wide range of Ub:UBQLN2 ratios (Fig 5A), as confirmed by turbidity plots (Fig 5B) and temperature-concentration phase diagrams (Fig 5C). Like K48-Ub4, the addition of K11-Ub4 largely disassembled UBQLN2 droplets. Strikingly, M1-Ub4 and HOTag6-G10-Ub stabilized UBQLN2 LLPS over a larger Ub:UBQLN2 range than K63-Ub4. Importantly, reentrant phase behavior, by which high concentrations of polyUb chains disassemble UBQLN2 droplets, still existed for all chains. As flexibility and propensity to adopt an extended conformation increased for polyUb (HOTag6-Ub > M1-Ub4 > K63-Ub4 > K48 or K11-Ub4), UBQLN2/polyUb LLPS was stabilized and promoted. These data bolster our hypothesis that more extended and flexible chains with more accessible Ub binding patches can promote UBQLN2 LLPS to a greater extent.

To determine how polyUb affect UBQLN2 concentration in the dilute and dense phases, we labeled UBQLN2 and Ub4 with organic dyes that absorb at different wavelengths. We induced UBQLN2 LLPS with Ub4 at different Ub:UBQLN2 ratios, centrifuged to separate the two phases, and measured the absorbance of the two dyes
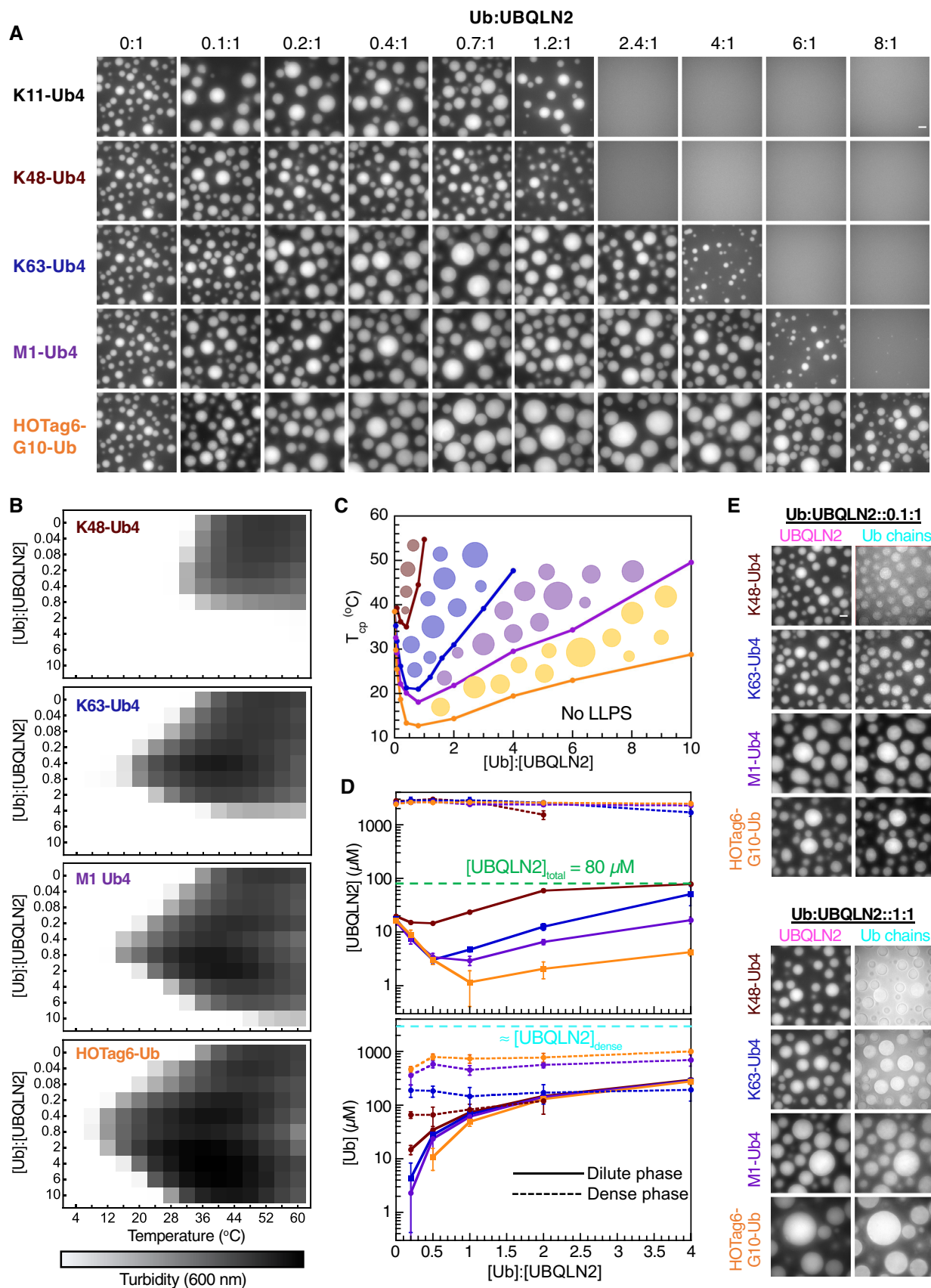
Figure 5.

Figure 5. The effects of polyUb chains on UBQLN2 LLPS are dependent on chain flexibility/accessibility to Ub-binding patch.

A   Fluorescence microscopy showing enhancement or inhibition of UBQLN2 droplet formation at increasing amounts of chains at 50 µM UBQLN2 in 20 mM NaPhosphate and 200 mM NaCl (pH 6.8) at 30°C. [Ub]:[UBQLN2] reflects the ratio between Ub monomers and UBQLN2 molecules. The solution is spiked with Alexa Fluor 647-labeled UBQLN2. The same image is used for the 0:1 condition. For visual comparison, images for K48-Ub4 and K63-Ub4 are identical to those shown in Fig 1A. Scale bar, 5 µm.

B   Representative results from spectrophotometric turbidity assay as a function of temperature at 30 µM UBQLN2.

C   Temperature–component phase diagrams showing the changes in LCST phase transition cloud point temperatures as a function of Ub:UBQLN2 for different Ub4 at 30 µM UBQLN2.

D   Phase diagrams showing the dense and dilute phase concentrations of UBQLN2 (top) and Ub chains (bottom). Error bars represent the standard deviation over three biological trials. Green dashed line (top) is the fixed total UBQLN2 concentration used (80 µM). For visual comparison, cyan dashed line (bottom) represents UBQLN2 concentration in the dense phase (> 2 mM) as determined from the top panel.

E   Fluorescence microscopy showing the distribution of Ub4 (spiked with Dylight 488-labeled chains) inside and outside droplets containing 50 µM UBQLN2 (spiked with Alexa Fluor 647-labeled UBQLN2). Scale bar, 5 µm.

Source data are available online for this figure.

to extract the dilute and dense phase concentrations of both UBQLN2 and Ub4 (see Methods, Fig 5D). The UBQLN2 dilute phase concentration, or c_{sat}, was entirely consistent with our phase diagrams (Fig 5C). In the presence of K48-Ub4, UBQLN2 c_{sat} barely changed at low Ub:UBQLN2 ratios but increased to total UBQLN2 concentration (only dilute phase existed) at high ratios. Conversely, at low Ub:UBQLN2 ratios for K63, M1-Ub4, and HOTag6-G10-Ub, c_{sat} significantly decreased before increasing again at high ratios. Effectively, the change in c_{sat} mirrored the UBQLN2/polyUb phase diagrams, in the order of increasing chain flexibility (Fig 4A). Intriguingly, although the addition of Ub4 significantly changed the UBQLN2 dilute phase concentration, the UBQLN2 dense phase concentration remained the same in the presence of any Ub4, regardless of Ub:UBQLN2 ratios. These data suggest that the addition of K48-Ub4, M1-Ub4 and HOTag6-G10-Ub chains regulates UBQLN2 LLPS by changing the volume fraction but not concentration, of the dense phase, consistent with a previous computational study for generic systems (Ruff *et al*, 2021a, 2021b). Therefore, HOTag6-G10-Ub and, to lesser extent, K63 and M1-Ub4 can enhance UBQLN2 LLPS without diluting the UBQLN2 dense-phase concentration over a wide range of polyUb ligand concentrations.

Unlike for UBQLN2, c_{sat} for Ub4 increased with increasing Ub:UBQLN2 ratios or total Ub concentrations (Fig 5D). At low ratios, c_{sat} for Ub4 were in the following order: K48-Ub4 > K63-Ub4 > M1-Ub4 > HOTag6-G10-Ub, indicating that HOTag6-G10-Ub is preferentially recruited to the dense phase and K48-Ub4 is the least likely to be in the dense phase. Consistently, the Ub4 dense phase concentrations followed the opposite trend of K48-Ub4 < K63-Ub4 < M1-Ub4 < HOTag6-G10-Ub. Interestingly, like for UBQLN2, the Ub dense phase concentrations did not vary with changing Ub:UBQLN2 ratios. However, to our surprise, the Ub:UBQLN2 ratio in the dense phase is much lower than 1:1. Even for HOTag6-G10-Ub, which has the highest dense phase concentration out of the four Ub4, the Ub:UBQLN2 ratio is only about 0.4:1. The substoichiometric Ub:UBQLN2 ratio inside the dense phase is maintained to at least 4:1 total Ub:UBQLN2 ratio (Fig 5D). These observations indicate that, at a given point, more than half of the UBQLN2 UBA sites are still unbound, i.e., free from ligand binding, in the dense phase. We surmise that Ub-unbound UBA stickers are still needed for interactions with other UBQLN2 regions to drive LLPS. UBQLN2 is a scaffold that undergoes LLPS via homotypic interactions. Upon heterotypic interactions with highly accessible and flexible multivalent ligands via its UBA stickers, UBQLN2 LLPS can be enhanced. Hence, the interplay between homotypic and heterotypic

interactions is essential for how multivalent ligands that bind to sticker sites on the scaffold can modulate LLPS.

The differential partitioning of UBQLN2 and Ub4 into dilute and dense phases can also be observed by fluorescence microscopy (Fig 5E). UBQLN2 localized mostly inside the droplets at both Ub:UBQLN2 ratios (0.1:1 and 1:1) for all four chains. However, at low Ub:UBQLN2 ratio (0.1:1), K63-Ub4, M1-Ub4, and HOTag6-G10-Ub were also mainly observed inside the droplets, whereas K48-Ub4 was only slightly enriched in the droplets compared with outside. In contrast, at higher Ub:UBQLN2 ratio (1:1), K63-Ub4, M1-Ub4, and HOTag6-G10-Ub were enriched inside the droplets, whereas K48-Ub4 was similarly distributed in the dense and dilute phases. These qualitative observations are entirely consistent with our measured values for the dilute and dense phase concentrations whereby K63-Ub4, M1-Ub4, and HOTag6-G10-Ub preferentially bind UBQLN2 in the dense phase and are recruited to UBQLN2 droplets. These three chains also slowed down the diffusivity dynamics of UBQLN2 in UBQLN2/chain condensates, as indicated by the increased fluorescence recovery after photobleaching (FRAP) half times (Appendix Fig S8A–D). The slowed dynamics likely resulted from these chains forming an interacting network with UBQLN2, preventing UBQLN2 from moving as freely inside the droplet. However, the three chains had little effects on droplet material properties, as indicated by the similar mobile fractions. K48-Ub4, which has little or no preference to be in UBQLN2 droplets, did not affect the dynamics or material properties of UBQLN2 droplets.

UBQLN2 condensates assemble during *in vitro* enzymatic assembly of K63-linked chains

Our data indicate that Ub and polyUb with different lengths and linkages can inhibit or enhance LLPS to different extents. However, in the cell, multiple Ub species, free and conjugated to substrate proteins, are in dynamic equilibrium with one another, depending on the cell cycle, cellular environment, and external stimuli (Park & Ryu, 2014). To test how changes in the distribution of different Ub species affect UBQLN2 LLPS, we devised a simplified system comprising 50 µM each of purified Ub and UBQLN2 (spiked with Dylight 650-labeled UBQLN2), and K63-specific ubiquitination machinery, including Ub-activating enzyme E1, and Ub-conjugating enzymes Mms2 and GST-Ubc13 (yeast version of UBE2V2-UBE2N). In the presence of MgCl$_2$, ATP, and TCEP at 37°C, the amount of free monoUb decreased slowly over time while K63-Ub2, Ub3, Ub4, and Ub5 chains were assembled as visible on the gel around 6, 9,

12, and 15 min, respectively (Fig 6A, lower left). Notably, after 27 min, free monoUb is still the predominant Ub species, as could be an equilibrium state for many cell types (Kaiser *et al*, 2011). To complement the monitoring of Ub chain formation by gel, we also observed the mixture under a microscope. At early time points, the solution was homogeneous but after about 15 min, micron-sized droplets appeared and grew bigger in size and number over time (Fig 6B; Movie EV1). As a negative control, no droplets were observed in that time frame without Ub in solution (Fig 6B) or in a solution with Ub and K48-specific ubiquitination machinery (Appendix Fig S9A and B). Therefore, even in the presence of a high ratio of free monoUb to K63-linked polyUb, UBQLN2 can still undergo LLPS as the ratio of different longer Ub chains increases.

Aside from the formation of free K63-linked polyUb chains, we also observed the possible formation of ubiquitinated GST-Ubc13 as the intensity of free GST-Ubc13 reduced over time (Fig 6A). Ub-binding proteins, like Ubc13, can be ubiquitinated in the presence of only E1 and E2 (Hoeller *et al*, 2007). There seemed to be several species of ubiquitinated GST-Ubc13, most likely monoubiquitinated at multiple lysine residues. We wondered if GST-Ubc13 could enter UBQLN2 condensates that form in the presence of K63-selective ubiquitination machinery. To test this, we set up the same experiment as above, spiked it with a small amount of Alexa Fluor 488-labeled GST-Ubc13, and observed droplet formation over time (Fig 6C). Excitingly, we could see slight enrichment of GST-Ubc13 in UBQLN2 droplets. Most GST-Ubc13 was not ubiquitinated and therefore not localized to UBQLN2 droplets. Ubiquitinated GST-Ubc13 seen here might act like a ubiquitinated substrate that can enter UBQLN2 droplets or even enhance UBQLN2 LLPS before being shuttled to the next step in a PQC pathway. Together, these data
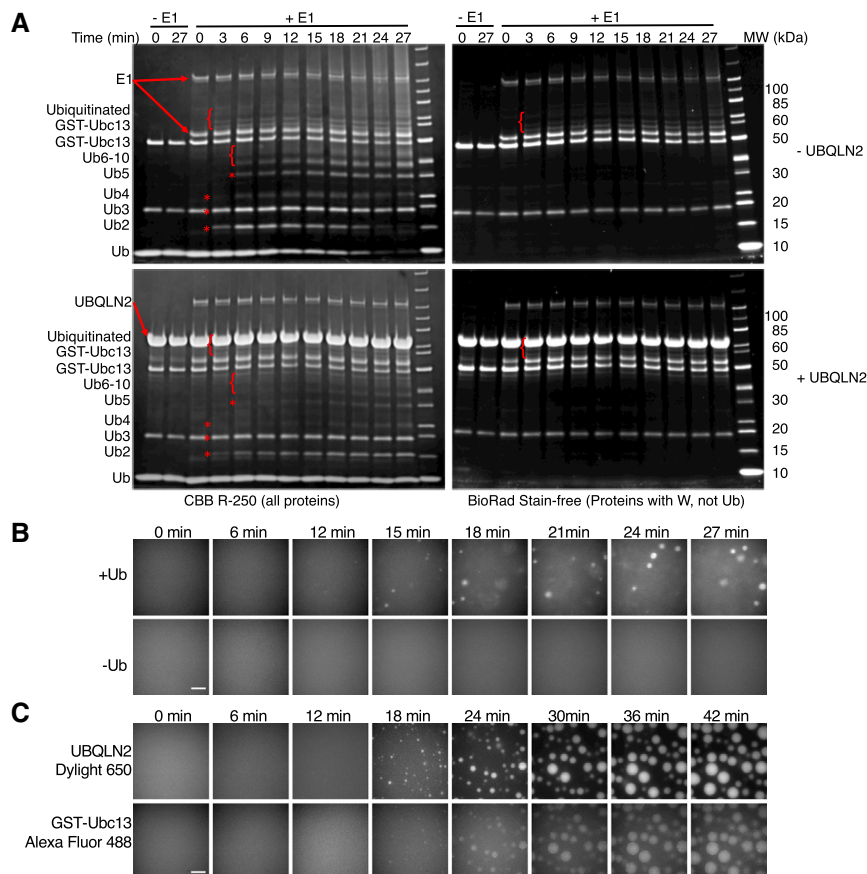

Figure 6. LLPS of UBQLN2 is induced during *in vitro* K63-selective ubiquitination assays.

A SDS–PAGE gels monitoring the formation of K63-linked polyUb chains and possibly ubiquitinated GST-Ubc13 over time, as indicated by asterisks and curly brackets. K63-Ub3 migrates on the gel similarly to His-Mms2, right below 20 kDa. Experimental conditions: ± 50 μM Ub and UBQLN2, 30 nM Dylight 650-labeled UBQLN2, 1 μM mE1, 2 μM His-Mms2, 4 μM GST-Ubc13, 10 mM ATP and MgCl₂, 3 mM TCEP, 50 mM Tris pH8, 37°C. The K63-linked polyUb chain reactions were done in the absence (top) and presence (bottom) of UBQLN2. Since UBQLN2 competes with E1 and E2 to bind to Ub, the presence of UBQLN2 slowed down chain formation (indicated by comparing disappearance rates of Ub). The band intensity for GST-Ubc13 decreased with time. The time-dependent appearance of species between 50 and 85 kDa was obstructed in the presence of UBQLN2. These species are most likely ubiquitinated GST-Ubc13, and not free polyUb chains, since these bands were observed with BioRad Stain-free gels (right) that detect proteins with tryptophan residues unlike Ub or polyUb chains.

B Time-lapse fluorescence microscopy monitoring UBQLN2 droplet formation in the presence of K63-selective ubiquitination machinery and with or without Ub. Experimental conditions were the same as in (A). Imaging was done in solution above the coverslip. Scale bar, 5 μm.

C Time-lapse fluorescence microscopy monitoring formation of UBQLN2- and GST-Ubc13-containing droplets in the presence of Ub and K63-selective ubiquitination machinery. Experimental conditions were the same as in (A) with the addition of 30 nM Alexa Fluor 488-labeled GST-Ubc13. Imaging was done at the coverslip surface. Scale bar, 5 μm.

indicate that a change in the equilibrium of Ub species (free, conjugated monoUb and polyUb chains) in response to a certain cellular signal can affect UBQLN2 LLPS ability, and perhaps functions in PQC.

Discussion

Recent studies have highlighted the important role of Ub and polyUb chains in modulating or driving LLPS of Ub-binding shuttle proteins hHR23B, UBQLN2, and p62 (Dao *et al*, 2018; Sun *et al*, 2018; Zaffagnini *et al*, 2018; Dao & Castañeda, 2020; Yasuda *et al*, 2020). However, these results appear to be at odds with each other. For example, K48-Ub4 mostly disassembles UBQLN2 droplets but drives hHR23B LLPS. Long K63 chains drive p62 LLPS but are much less effective at driving hHR23B LLPS compared with K48 chains. Our mechanistic understanding of how five types of polyUb chains interact with UBQLN2 reconcile these differences and, together with other studies, offer general principles governing the driving force of polyUb chains on shuttle protein LLPS.

We showed that K48-linked chains of four or fewer Ub units generally inhibited or barely enhanced UBQLN2 LLPS, whereas K63-linked chains enhanced LLPS over a wide range of Ub:UBQLN2 ratios. We postulated that differences in either chain conformations or binding affinities among UBQLN2 and these chains lead to these different behaviors. We demonstrated, using additional K11, M1-Ub4 chains, and HOTag6-G10-Ub, that more extended chains with easily accessible Ub hydrophobic patches can readily promote UBQLN2 LLPS. K63- and M1-linked chains also stabilize LLPS with other proteins, such as p62 (Sun *et al*, 2018; Zaffagnini *et al*, 2018). Even though K_d values for UBQLN2 and K48-Ub4 differed significantly, depending on the methods employed and whether the labeled partner was UBQLN2 or K48-Ub4, we believe, together with results for K11-Ub4, that these differences stemmed from the compact conformation of K48-Ub4, which has to open for UBQLN2 binding. Moreover, although the binding affinities between UBQLN2 and HOTag6-G10-Ub, M1-Ub4, and K63-Ub4 were similar (Fig 4G), HOTag6-G10-Ub greatly reduced c_{sat} for UBQLN2 compared with K63-Ub4. Therefore, our data suggested that binding affinities do not contribute significantly to the differences in the effects of polyUb chains on UBQLN2 LLPS.

Interestingly, pulldowns of K48- and K63-linked chains using GST-tagged UBQLN1, a close UBQLN2 homolog that also undergoes LLPS (Gerson *et al*, 2021), show that FL UBQLN1 only interacts with longer K63-linked chains (Harman & Monteiro, 2019). However, UBQLN1 and UBQLN2 UBAs have no significant preference for either chain (Fig 4G) (Raasi *et al*, 2005; Zhang *et al*, 2008). We speculate that K63-, but not K48-linked, chains undergo LLPS with UBQLN1 during the pulldown process and thus appear to be a tighter binding partner. Like UBQLN2, p62 preferentially phase separates with K63- and M1-linked chains (Sun *et al*, 2018; Zaffagnini *et al*, 2018). Also like UBQLN2, FL p62 can only bind to K63-linked chains through pulldown assays (Cabe *et al*, 2018), whereas p62 UBA bind to both chains with similar affinities (Raasi *et al*, 2005; Long *et al*, 2008). Could the preferential pulldown of K63-linked chains by p62 also be an artifact of LLPS? Direct determination of binding affinities and mechanisms between p62 and these chains is needed to tease out the contributions of chain

conformation and binding affinity to differences in how p62 phase separates in the presence of different chains. Unlike UBQLN2 and p62, hHR23B appears to bind more tightly to and phase separates preferentially with K48-linked chains than K63-linked chains (Raasi *et al*, 2005; Nathan *et al*, 2013; Yasuda *et al*, 2020). We do note that affinities between hHR23B and polyUb chains need to be confirmed via multiple techniques in light of our conflicting NMR and anisotropy results. Phase diagrams under multiple conditions are needed to conclusively state that K48-linked chains are more efficient at driving hHR23B LLPS. Together, these data indicate that when binding affinities are similar, extended chains with easily accessible Ub hydrophobic patches can stabilize LLPS of Ub-binding shuttle proteins more efficiently. However, preferential binding between a shuttle protein and a compact chain might compensate for the chain's less extended structure and promote LLPS more efficiently. Moreover, our "designed Ub4," HOTag6-G_{10}-Ub with a long linker between HOTag6 and individual Ub units, resembles a multi-monoubiquitinated substrate. Therefore, substrates that are post-translationally modified with multi-monoubiquitination could drive UBQLN2 LLPS and potentially other Ub-binding adaptor proteins.

Through promoting or inhibiting LLPS, polyUb chains could be potent modulators of signaling outcomes in the cell, akin to PARylation, another PTM that regulates LLPS via length and branching (Reber & Mangerich, 2021). For example, both K11- and K48-linked chains are linked to proteasomal degradation pathways, with a branched K11/K48 chain binding more tightly to the proteasome (Boughton *et al*, 2019). Intriguingly, only these chain types destabilize UBQLN2 LLPS. In contrast, K63- and M1-linked polyUb are typically involved in nonproteolytic signaling pathways such as cargo sorting, DNA repair, NF-Kβ signaling, and autophagy (Olzmann *et al*, 2007; Haglund & Dikic, 2012; Linares *et al*, 2013; Piper *et al*, 2014; Sun *et al*, 2018). UBQLN2 has known affiliations with the proteasome, autophagy receptors (LC3) and cargo sorting adaptor proteins (epsin 1 and 2) (Zheng *et al*, 2020; Lin *et al*, 2021). We showed that UBQLN2 LLPS can be rapidly modulated by changes in cellular signaling (e.g., formation of K63-linked chains or ubiquitinated substrates, Fig 6). The UBQLN2 concentration in cells could be below the threshold needed for LLPS such that UBQLN2 is diffuse under normal conditions. In response to a cellular event, such as stress, substrates can be ubiquitinated and elicit different responses from UBQLN2, depending on the types of ubiquitination (Fig. 7A and B). UBQLN2 can bind to K11- or K48-linked ubiquitinated substrates, stay diffuse, and shuttle substrates to the proteasome for degradation. UBQLN2 can bind to K63- or M1-linked substrates, colocalize to, or form substrate-containing condensates. These condensates can be similar to p62- or hHR23B-containing nuclear degradation foci to which proteasomes are recruited (Yasuda *et al*, 2020; Fu *et al*, 2021) or initiation centers for the formation of autophagosomes (Sun *et al*, 2018; Zaffagnini *et al*, 2018; Turco *et al*, 2019). The polyUb effects on UBQLN2 LLPS may be the general mechanism regulating the roles of UBQLN2 and other Ub-binding shuttle proteins in the cell.

UBQLN2 is also recruited to stress granules, most likely due to its LLPS properties (Alexander *et al*, 2018; Dao *et al*, 2018). UBQLN2 expression levels are negatively correlated to the number and sizes of stress granules (Alexander *et al*, 2018), indicating a role for UBQLN2 in regulating the disassembly of stress granules. Stress granules are cleared either following the removal of K63-linked
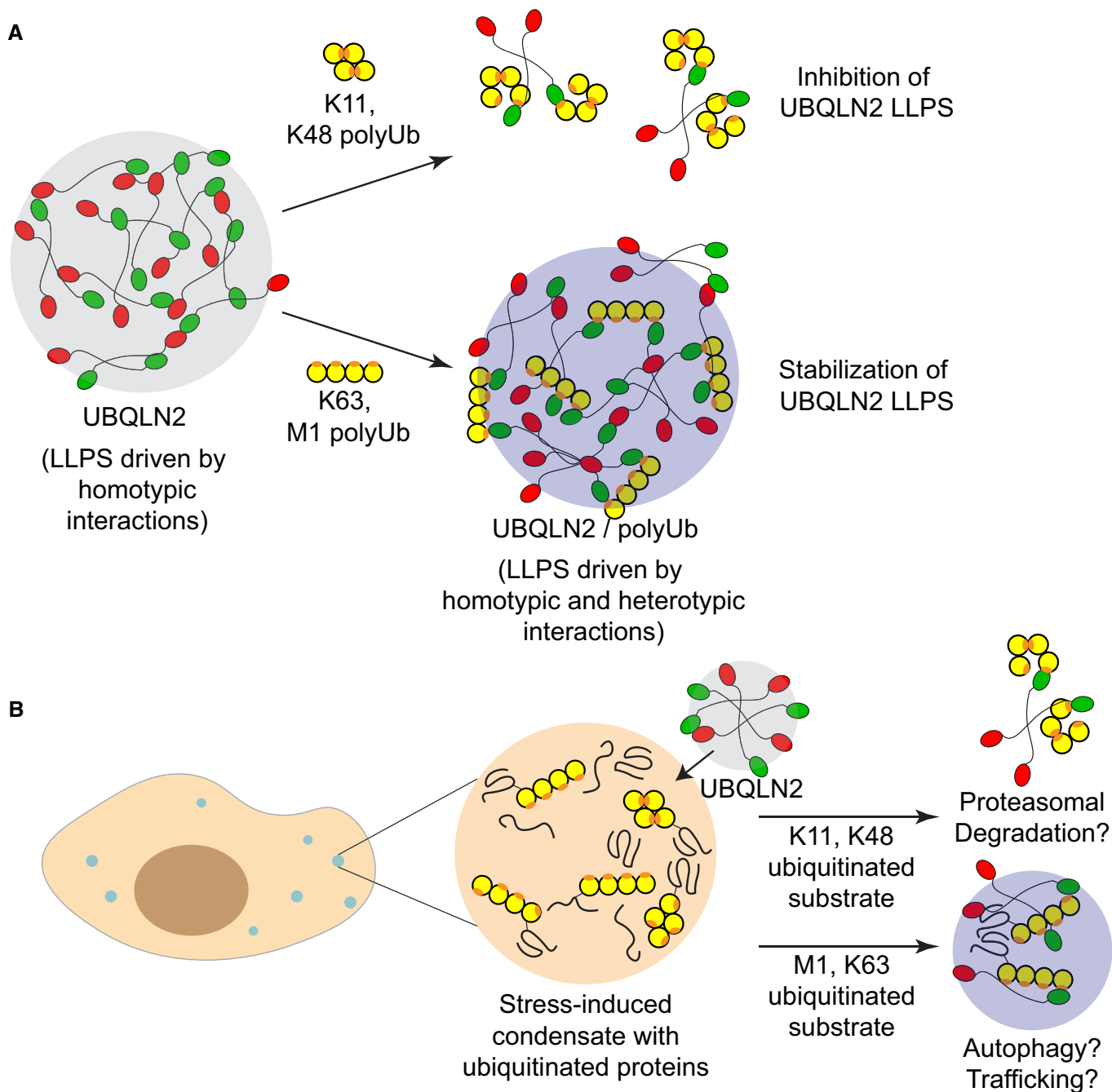
Figure 7. PolyUb chains either inhibit or stabilize LLPS via heterotypic interactions.

A Compact polyUb chains (e.g., K11, K48) generally inhibit UBQLN2 LLPS, whereas extended chains with accessible hydrophobic patches promote heterotypic LLPS. Orange hotspots on Ub units indicate a hydrophobic patch.

B Model for how polyUb-modulated effects on LLPS may drive different cellular outcomes and signal different PQC pathways for ubiquitinated proteins in stress-induced condensates. K11 and K48 chains typically signal for proteasomal degradation, whereas extended K63 and M1 chains are implicated in autophagy and other nonproteolytic pathways.

polyubiquitinated G3BP1, a stress granule core protein, or by autophagy, depending on the stressor types and length of exposure (Buchan *et al*, 2013; Gwon *et al*, 2021). Through differential modulation of UBQLN2 LLPS by different polyUb chains, UBQLN2 may facilitate these different stress granule clearance processes (Fig 7B). Persistent stress granules can lead to the formation of disease-linked protein-containing inclusions (Nedelsky & Taylor, 2019), that comprise, among others, PQC components such as UBQLN2 and

polyUb chains (Deng *et al*, 2011; Ceballos-Diaz *et al*, 2015; Sharkey *et al*, 2020). Therefore, knowledge of how polyUb chains affect UBQLN2 in stress granules is essential to understanding the cellular functions of UBQLN2.

Aside from cellular implications, our work presented here also contributes to the important question of how binding to multivalent ligands modulates the phase boundaries of phase-separating systems. Using monovalent and divalent ligands, Ruff and colleagues demonstrated through simulations that high-valency ligands that bind more tightly to spacer sites (residues or protein regions not involved in driving LLPS) are more effective at lowering the c_{sat} necessary for LLPS of multivalent scaffolds (Ruff *et al*, 2021a). Conversely, ligands that bind to sticker sites generally increase c_{sat}, but the effect is lessened with increasing ligand valency. Our experimental work recapitulates many of these observations and offers additional insights. We systematically and quantitatively demonstrated that longer polyUb could either less effectively inhibit (K48 chains) or more effectively promote (K63 chains) UBQLN2 LLPS (Fig 1). In fact, K48-Ub4 slightly promoted UBQLN2 LLPS at low Ub:UBQLN2 ratios. Following this trend, K48 chains with five or more Ub units would further enhance UBQLN2 LLPS, in a similar manner as K63 chains with 3 or 4 Ub units. K48 and K63 polyUb ligands interact mainly with UBQLN2 UBA stickers, but K48-linked chains also interact with an additional sticker site. Therefore, K48 chains need to have increased valency (by increasing chain length) to compensate for the loss of a sticker site important for UBQLN2 self-interactions and LLPS. We expect multivalent ligands that bind to sticker sites of other systems to enhance LLPS when a certain ligand valency is reached.

Despite having the same valency and binding to the same UBQLN2 stickers (Fig 4C) with similar affinities (Fig 4H), the ligands K63-Ub4, M1-Ub4, and HOTag6-G10-Ub lower c_{sat} for UBQLN2 LLPS to highly different extents (Fig 5D). The major difference among these chains is how the UBQLN2-binding surface is presented (i.e., the spacer length and flexibility between the stickers). Therefore, how a multivalent ligand modulates LLPS of a scaffold (e.g., UBQLN2) depends not only on binding affinities, ligand valencies, and binding sites on the scaffold but also on the properties of the spacers between the stickers on the ligand. In our case, it appears that longer, more flexible spacers are better at promoting LLPS, likely due to the ligand generating a broader interacting network. However, there must be a limit after which the multivalent ligand begins to behave like individual units of monovalent ligands. It would be interesting to determine what that limit is in terms of spacer length/flexibility and if this principle can be generalized to other systems.

Overall, we uncovered the molecular mechanisms enabling distinct polyUb chains to be potent regulators of phase separation of UBQLN2 and possibly other Ub-binding shuttle proteins. With this knowledge, we can design specific experiments in cells, such as inhibition of certain polyUb chains or PQC pathways, to elicit how polyUb chains may tune UBQLN2's ability to form or be recruited into condensates and then carry out PQC functions. Moreover, disease mutations in UBQLN2 have been shown to disrupt UBQLN2's roles in PQC (Hjerpe *et al*, 2016; Chen *et al*, 2018; Halloran *et al*, 2020). Therefore, determining the effects of polyUb chains on the phase separation of UBQLN2 variants is an essential next step to elucidating disease-related mechanisms involving UBQLN2.

Materials and Methods

Gene synthesis and site-directed mutagenesis

The HOTag6-G10-Ub polypeptide has the following sequence: MTLREIEEELLRKIIEDSVRSVA ELEDIEKWLKKIGGGGGGGGGGMQIF VKTLTGKTITLEVEPSDTIENVKAKIQDKEGIPPDQQRLIFAGKQLEDG RTLSDYNIQKESTLHLVLRLRGG. The genes encoding HOTag6-G10-Ub and M1-Ub4-His6 were codon-optimized, synthesized, and cloned into pET24b (Novagen) by GenScript (NJ, USA). K48R, K63R, K11/63R Ub, and Ub-V-His6 were made using Phusion Site-Directed Mutagenesis Kit (Thermo Scientific).

Protein expression, and purification

Wildtype, K48R, K63R, Ub, and Ub-V-His6 were expressed and purified as detailed elsewhere (Beal *et al*, 1996; Castañeda *et al*, 2016b). The gene encoding mouse E1 was a kind gift from Jorge Eduardo Azevedo (Addgene plasmid 32,534; Carvalho *et al*, 2011). E1, Mms2, Yuh1, and GST-Ubc13 were expressed in *Escherichia coli* NiCo21 (DE3) cells in Luria-Bertani (LB) broth at 16°C overnight. GST-E2-25K in pGEX-4 T2 and GST-Ube2s-UBD in pGEX6P1 were expressed in Escherichia coli Rosetta 2 (DE3) pLysS cells in Luria-Bertani (LB) broth at 16°C overnight. Bacteria were pelleted, frozen, then lysed via freeze/thaw method in 50 mM Tris, 1 mM EDTA (pH 8), 1 mM PMSF, 1 mM MgCl$_2$, and 25 U of Pierce universal nuclease. Yuh1, E1, and Mms2 were purified via Ni^{2+} affinity chromatography. GST-E2-25K, GST-Ubc13, and GST-Ube2s-UBD were purified via GST chromatography. All proteins were concentrated, buffer exchanged into 50 mM Tris and 1 mM EDTA (pH 8), and stored at 80°C for subsequent use in the production of K48- and K63-linked polyUb chains, and K11-linked Ub4.

K48-linked and K63-linked Ub2, Ub3, and Ub4 were synthesized sequentially. Briefly, equal amounts of K48R (K63R) Ub and Ub-V-His6 incubated with 1,000 nM E1 and 10 μM GST-E2-25K (2 μM His-Mms2 and 4 μM GST-Ubc13) in the presence of 10 mM ATP, 0.3 mM TCEP in Tris buffer at pH 8 for 3 h at 37°C. This procedure generates K48R (K63R) Ub2 with the C-terminal end of the proximal Ub blocked by V-His6. Yuh1 was added to remove the V-His6 from the end of Ub2, which was then purified via cation exchange column using 50 mM ammonium acetate (pH 4.5) as the buffer. Protein was eluted via a linear gradient from 0 to 100% of 50 mM ammonium acetate, 1 M NaCl (pH 4.5). Purified Ub2 was then buffer exchanged into 50 mM Tris buffer at pH 8. K48 and K63-Ub3 were made the same way Ub2 was made. K48 and K63-Ub4 required an additional purification step via size exclusion chromatography using a Superdex 75 HiLoad 16/600 column (GE Healthcare). K11-Ub2 was made with K63R as described by (Bremm *et al*, 2010) using mE1 and GST-Ube2s-UBD in similar conditions as for K48 and K63 chains. K11-Ub4 was made from K11-Ub2 and purified by size exclusion chromatography using a Superdex 75 HiLoad 16/600 column (GE Healthcare). The yield for K11-Ub4 was about 10%, much lower than for K48 and K63-Ub4, which was about 50%.

HOTag6-G10-Ub and M1-Ub4-His6 were expressed in *Escherichia coli* NiCo21 (DE3) cells in Luria-Bertani (LB) broth at 37°C overnight. Bacteria were pelleted, frozen, then lysed via freeze/thaw method in 50 mM Tris, 1 mM EDTA (pH 8), 1 mM PMSF, 1 mM MgCl$_2$, and 25 U of Pierce universal nuclease. The cleared lysate for

HOTag6-G10-Ub was then loaded onto anion exchange column and eluted with a gradient between 20 mM HEPES, 0.02% NaN$_3$ (pH 7), and 20 mM HEPES (pH 7), 1 M NaCl, 0.02% NaN$_3$. Fractions containing HOTag6-G10-Ub were dialyzed, loaded onto a cation exchange column, and eluted with a gradient between 50 mM ammonium acetate (pH 4.5) and 50 mM ammonium acetate, 1 M NaCl (pH 4.5). Purified HOTag6-G10-Ub was then concentrated, and buffer exchanged into 20 mM NaPhosphate, 0.5 mM EDTA, 0.1 mM TCEP, 0.02% NaN$_3$ (pH 6.8). M1-Ub4-His6 was purified via Ni^{2+} chromatography and dialyzed into 50 mM Tris, 1 mM DTT before the addition of Yuh1 to cleave the His-tag after the last Ub unit. The cleaved M1-Ub4 was then dialyzed into 50 mM ammonium acetate pH 4.5, loaded onto cation exchange column, and eluted with a gradient between 50 mM ammonium acetate (pH 4.5) and 50 mM ammonium acetate, 1 M NaCl (pH 4.5). The fractions containing M1-Ub4 were concentrated and exchanged into 20 mM NaPhosphate, 0.5 mM EDTA, 0.1 mM TCEP, 0.02% NaN$_3$ (pH 6.8). Purified proteins were frozen at −80°C.

Full-length UBQLN2 and UBQLN2 450–624 were expressed and purified as described previously (Dao *et al*, 2018). Briefly, the constructs were expressed in *E. coli* Rosetta 2 (DE3) pLysS cells in Luria-Bertani (LB) broth at 37°C overnight. Bacteria were pelleted, frozen, lysed, then purified via a "salting out" process. NaCl was added to the cleared lysate to the final concentration of 0.5–1 M. UBQLN2 droplets were pelleted and then resuspended in 20 mM NaPhosphate, 0.5 mM EDTA, 0.1 mM TCEP, 0.02% NaN$_3$ (pH 6.8). Leftover NaCl was removed through HiTrap desalting column (GE Healthcare). Purified proteins were frozen at −80°C.

Fluorescent labeling

For imaging, determination of dense and dilute phase concentrations, and FRAP experiments, UBQLN2, GST-Ubc13, K48-Ub4, K63-Ub4, M1-Ub4, and HOTag6-G10-Ub constructs were fluorescently labeled with Dylight-488, DyLight-650 (Thermo Scientific), or Alexa Fluor-488 NHS Ester (Molecular Probes), according to the manufacturer's instructions. For fluorescence anisotropy experiments, UBQLN2 450–624 with an S624C mutation, K48-Ub4, and K63-Ub4 with an S20C mutation on the most distal Ub were fluorescently labeled with Alexa Fluor 488 C$_5$ Maleimide (Invitrogen). Excess dye was removed via size exclusion chromatography using an ENrich™ SEC 650 10 × 300 Column (BioRad).

Spectrophotometric absorbance/turbidity measurements

Protein samples were prepared by mixing protein solution containing UBQLN2 and polyUb (the concentrations of the protein stock solutions were doubled compared with the sample concentrations) and cold sodium phosphate buffer (pH 6.8, 20 mM NaPhosphate, 0.5 mM EDTA, 0.1 mM TCEP, 0.02% NaN$_3$) containing 400 mM NaCl at 1:1 stoichiometry. The protein concentrations were chosen to cover as wide a range as possible to allow observation of phase separation during the temperature ramps. All the solutions were kept on ice for at least 5 min before mixing. Absorbance at 600 nm was recorded as a function of temperature by a Cary 3500 UV–Vis spectrophotometer using a temperature ramp rate of 1°C/min increasing from 16 to 60°C (4 to 60°C range was screened in some cases). Net absorbance values were recorded after subtracting the

absorbance value of buffer control. Data were plotted using Mathematica (Wolfram Research).

Phase diagram measurements

For the LCST (lower critical solution temperature) phase transition, i.e., mapping the phase boundary as the temperature is increased, protein samples were prepared as described for the turbidity measurements. Cloud point temperatures were determined by fitting a four-parameter logistic regression model to the data:

$$y = d + \frac{a-d}{1 + \left(\frac{x}{c}\right)^b} \tag{1}$$

Cloud point temperatures (T$_{cp}$) used were the points of inflection (c). Cloud point temperatures were used to define the coexistence curve as a function of ligand:protein ratio (ligand refers to polyUb chains and protein refers to UBQLN2). Fitting and plotting of data were done with Mathematica (Wolfram Research) and Kaleidagraph (Synergy Software).

Bright-field imaging of phase separation

Samples were prepared to contain 50 µM UBQLN2 and different amounts of Ub and Ub chains in 20 mM NaPhosphate, 200 mM NaCl, 0.1 mM TCEP, and 0.5 mM EDTA (pH 6.8), spiked with UBQLN2 labeled with Dylight 650 and/or Ub chains labeled with Dylight 488. Samples were added to Eisco Labs Microscope Slides, with Single Concavity, and covered with MatTek coverslips that had been coated with 5% bovine serum albumin (BSA) to minimize changes due to surface interactions, and incubated coverslip-side down at 30°C for 10 min. Phase separation was imaged on an ONI Nanoimager (Oxford Nanoimaging Ltd, Oxford, UK) equipped with a Hamamatsu sCMOS ORCA flash 4.0 V3 camera using an Olympus 100×/1.4 N.A. objective. Images were prepared using Fiji (Schindelin *et al*, 2012) and FigureJ plugin.

Calculations of dilute and dense phase concentrations

Samples were prepared on ice to contain 50 µl of 70 µM UBQLN2, 10 µM of UBQLN2 labeled with Alexa Fluor 488, 5 µM of Ub or Ub chains labeled with Dylight 650, and different amounts of Ub and Ub chains in 20 mM NaPhosphate, 200 mM NaCl, 0.1 mM TCEP, and 0.5 mM EDTA (pH 6.8). Samples were incubated at 30°C for 10 min, then centrifuged at 10,000 *g* for 5 min at 30°C. Without disrupting the pellet, as much of the supernatant as possible was transferred to a new tube. 8 µl of 8 M urea solution was added to the pellet. The tube containing pellet and urea was incubated for 1 h at room temperature, vortexed, and centrifuged. The volume of the mixture was determined by pipetting with a P10. The dense phase volume was determined by subtracting the total volume by 8 µl of urea added. Absorbance at 493 nm (for Alexa Fluor 488/ UBQLN2) and 655 nm (for Dylight 650/Ub chains) was recorded. Dense and dilute phase concentrations were determined with a standard curve for multiple concentrations of UBQLN2 mixed with UBQLN2 labeled with Alexa Fluor 488 and Ub chains mixed with Ub chains labeled with Dylight 650.

Fluorescence recovery after photobleaching (FRAP)

To perform FRAP on UBQLN2/Ub chain droplets of similar size, samples were prepared to contain different UBQLN2 concentrations, depending on Ub chain types and molar ratios, in 20 mM NaPhosphate, 200 mM NaCl, 0.1 mM TCEP, and 0.5 mM EDTA (pH 6.8). Specifically, for UBQLN2-only K48-Ub4/UBQLN2 at 1:1 samples, UBQLN2 concentration is 60 μM. For K48-Ub4/UBQLN2 at 1:1, UBQLN2 concentration is 75 μM. For K63-Ub4/UBQLN2 at 0.5:1 and 1:1, UBQLN2 concentration is 50 μM. For K63-Ub4/UBQLN2 at 2:1, UBQLN2 concentration is 60 μM. For M1-Ub4/UBQLN2 at 0.5:1 and 1:1, UBQLN2 concentration is 40 μM. For M1 Ub4/UBQLN2 at 2:1, UBQLN2 concentration is 50 μM. For HOTag6-Ub/UBQLN2 at 0.5:1 and 1:1 and 2:1, UBQLN2 concentration is 30 μM. Samples were added to Eisco Labs Microscope Slides, with Single Concavity, and covered with MatTek coverslips that had been coated with 5% bovine serum albumin (BSA), and incubated coverslip-side down at 30°C for 20–30 min. FRAP was carried on a Zeiss LSM 980 with Airyscan 2 confocal microscope (Carl Zeiss AG, Oberkochen, Germany) using a Plan-Apochromat 63X/1.4 NA oil. Images were prepared using Fiji (Schindelin *et al*, 2012) and FigureJ plugin.

NMR spectroscopy

Proteins were prepared in 20 mM NaPhosphate buffer (pH 6.8), 0.5 mM EDTA, 0.02% NaN$_3$, and 5% D$_2$O. ^{1}H-^{15}N SOFAST-HMQC was used for titration experiments of UBQLN2 constructs and polyUb, although additional ^{1}H-^{15}N TROSY-HSQC experiments were collected at distinct Ub:UBQLN2 ratios. ^{1}H-^{15}N TROSY-HSQC experiments were used for experiments involving full-length UBQLN2. All NMR experiments were performed on a Bruker Avance III 800 MHz spectrometer equipped with a TCI cryoprobe at 25°C. ^{1}H-^{15}N SOFAST-HMQC experiments were acquired using spectral widths of 16 and 30 ppm in the direct ^{1}H and indirect ^{15}N dimensions, using 2048 and 160 total points, respectively. NMRPipe (Delaglio *et al*, 1995) was used to process all NMR data, and peak analyses were performed using CCPNMR 2.5 (Vranken *et al*, 2005). Chemical shift perturbations (CSPs) were quantified as follows:

$$\Delta\delta = \left[(\Delta\delta_H)^2 + (\Delta\delta_N/5)^2 \right]^{1/2} \qquad (2)$$

where $\Delta\delta_H$ and $\Delta\delta_N$ are the differences in ^{1}H and ^{15}N chemical shifts, respectively.

NMR titration experiments and K$_d$ determination

Unlabeled protein ligand (Ub4 in most cases) was titrated into 50 μM samples of ^{15}N-labeled protein (UBQLN2), and the binding was monitored by recording ^{1}H-^{15}N TROSY-HSQC or SOFAST-HMQC spectra as a function of ligand:protein ratios of concentrations. Concentrations of Ub ligand were adjusted by the number of Ub units in the polyUb chain such that 50 μM Ub4 was equal to 200 μM Ub. For TITAN (Waudby *et al*, 2016) lineshape analysis, only SOFAST-HMQC spectra for titrations involving ^{15}N-labeled protein (UBQLN2 450–624) were used, following the NMR processing protocol in (Waudby & Christodoulou, 2020). TITAN software was used within NMRbox (Maciejewski *et al*, 2017). For all cases, the single-site binding model (two-state ligand binding in TITAN)

was used. Parameters were first estimated using a K$_d$ of 10 μM and a k$_{off}$ rate of 5,000 s^{-1}. Binding affinity calculations were performed using global fitting of peaks from a total of 10–12 amide resonances (Appendix Fig S6A–F). We evaluated how well the peaks were fit using two-dimensional contour maps and removed poorly fit peaks (typically in crowded areas of the spectrum). Once complete, errors were evaluated using jackknife analysis; the representative best fit of spectra is shown in Appendix Fig S6.

Sedimentation velocity analytical ultracentrifugation

Purified UBQLN2 487–624, K48-Ub4, K63-Ub4, or UBQLN2:Ub4 complexes were loaded into 3- or 12-mm two-sector charcoal-filled Epon centerpieces with sapphire windows. All experiments were carried out using a Beckman Coulter ProteomeLab XL-A analytical ultracentrifuge equipped with absorbance optics and a 4-hole An-60 Ti rotor at 289,786 *g* that was pre-equilibrated to 20°C prior to running the experiment. The samples were scanned with a zero-second time interval between scans for 300 scans and analyzed by the continuous distribution ($c(s)$) method in the program SEDFIT (Schuck, 2000). Concentration profiles ($a(r,t)$) were modeled as the sum of Lamm Equation solutions scaled by a continuous distribution $c(s)$ as follows:

$$a(r,t) \cong \int_{S_{min}}^{S_{max}} c(s)\chi(s,D(s),r,t)ds, \qquad (3)$$

where s is the sedimentation coefficient, $\chi(s,D(s),r,t)$ is the Lamm Equation solution that is dependent on $D(s)$, the corresponding diffusion coefficient, r, radius from the center of rotation, and t, the time from the beginning of the experiment (Schuck, 2000; Padrick & Brautigam, 2011). The program SEDNTERP (Laue *et al*, 1992) was used to calculate the buffer density (1.0064 ml/g), viscosity (0.009 *P*), and partial specific volume of UBQLN2 ($\bar{v}$ = 0.7281), K48-Ub4 (0.746), K63-Ub4 (0.746), K48-Ub4 + UBQLN2 (0.7405), and K63-Ub4 + UBQLN2 (0.7426), which were based on the amino acid sequences.

Multisignal sedimentation velocity (MSSV) analysis was performed to determine the stoichiometry of the complex formed between UBQLN2 and Ub4. In MSSV, the standard $c(s)$ approach is modified to deconvolute the contributions of individual species with distinct spectral properties in a component distribution $c_k(s)$ where k represents the individual components of a mixture. Here, the absorbance at wavelength λ ($a_\lambda(r,t)$) is modeled as:

$$a_\lambda(r,t) \cong \sum_{k=1}^{K} \epsilon_\lambda^k l \int_{S_{min}}^{S_{max}} c_k(s)\chi(s,D_k(s),r,t)ds \qquad (4)$$

where l is the path length, K is the number of solutes present, and $c_k(s)$ is a continuous distribution for component k. The spectral properties of the individual proteins were first determined by SV-AUC using absorbance at 260 nm and 280 nm. Global component $c_k(s)$ analysis of both signals was performed using the known ϵ^{280} extinction coefficient as a reference to calibrate ϵ^{260} for each protein (Appendix Table S4). The results indicate good spectral discrimination between UBQLN2 and both Ub4s with fitted spectral discrimination parameter D$_{norm}$ > 0.236 (Brautigam *et al*, 2013). MSSV of the UBQLN2:Ub4 mixtures were then

collected at both 260 nm and 280 nm and globally fit using the multiwavelength discrete/continuous distribution analysis with mass constraints in SEDPHAT version 15-2b. Integration of the resulting $c_k(s)$ distributions revealed the molar signal increment for each protein under a peak at a given sedimentation value (Appendix Fig S4). All plots were created with GUSSI (Brautigam, 2015).

To determine the statistical significance of the resulting molar ratios, global $c_k(s)$ analyses were conducted by constraining the molar ratio to different values and determining whether the resulting fit to the data χ_t^2 is significantly worse than the unconstrained analysis χ^2, using the built-in F-statistics calculator to determine the critical χ^2 at 1σ and 2σ. Fixed molar ratios with χ_t^2 values exceeding the critical χ^2 value at 2σ (dashed red line in Appendix Fig S4) were deemed significantly different from that of the unconstrained analysis and rejected (Padrick & Brautigam, 2011).

Fluorescence polarization anisotropy

Fluorescence anisotropy measurements were made on a SpectraMax i3x plate reader (Molecular Devices) with the FP-FLUO settings. Experiments were done using 100 nM fluor-UBQLN2 450–624 in 20 mM sodium phosphate buffer, 0.5 mM EDTA, pH 6.8 at 25°C containing 10 µM BSA to reduce protein sticking to the plate. Ub or Ub chains were prepared in the same solution at 150 µM Ub (M1-Ub4, HOTag6-Ub), or 50 µM Ub (K48-Ub4 and K63-Ub4), or 50 µM Ub (K11-Ub4), and 1.5-fold, or 1.5-fold, or 2-fold serial dilutions, respectively, were prepared in the 96-well plate (100 µl per well, read height 1.18 mm). Reciprocal experiments were done using 100 nM fluor-K48-Ub4 or fluor-K63-Ub4 and 50 µM UBQLN2 450–624 in 2-fold serial dilutions. A single-site binding equation was used to fit anisotropy data as a function of Ub concentration:

$$r = r_F + (r_B - r_F)\frac{[fluor] + K_d + x - \sqrt{(x + K_d + [fluor])^2 - 4[fluor]x}}{2[fluor]}$$

(5)

where x is ligand concentration, $[fluor]$ is the concentration of fluor-UBQLN2 450–624 or fluor-K48-Ub4 or fluor-K63-Ub4 (100 nM for all titrations), r is the observed anisotropy, r_F is the anisotropy at zero ligand concentration and r_B is the anisotropy at saturating ligand concentration. K_d was determined from an average of three replicates. Fitting and plotting were done with Kaleidagraph (Synergy Software).

SEC-MALS-SAXS experiments

SAXS was performed at BioCAT (beamline 18ID at the Advanced Photon Source, Chicago) with in-line size exclusion chromatography (SEC) to separate samples from aggregates and other contaminants thus ensuring optimal sample quality and multiangle light scattering (MALS), dynamic light scattering (DLS) and refractive index measurement (RI)) for additional biophysical characterization (SEC-MALS-SAXS). All protein samples were prepared in 20 mM NaPhosphate buffer at pH 6.8 containing 0.5 mM EDTA and 0.02% NaN₃ (See Appendix Table S4 for details). The samples were loaded on a Superdex 200 10/300 Increase column (Cytiva) at a temperature of 20°C run by a 1260 Infinity II HPLC (Agilent Technologies) at 0.6 ml/min. The flow passed through (in order) the Agilent UV detector, a MALS detector and a DLS detector (DAWN Helios II, Wyatt Technologies), and an RI detector (Optilab T-rEX, Wyatt). The flow then went through the SAXS flow cell. The flow cell consists of a 1.0 mm ID quartz capillary with ~20 µm walls. A coflowing buffer sheath is used to separate sample from the capillary walls, helping prevent radiation damage (Kirby *et al*, 2016). Scattering intensity was recorded using a Pilatus3 X 1 M (Dectris) detector which was placed 3.6 m from the sample giving us access to a q-range of 0.003 Å⁻¹ to 0.35 Å⁻¹. 0.5 s exposures were acquired every 2 s during elution, and data were reduced using BioXTAS RAW 2.1.1 (Hopkins *et al*, 2017). Buffer blanks were created by averaging regions flanking the elution peak (see Appendix Fig S5A) and subtracted from exposures selected from the elution peak to create the I(q) vs. q curves used for subsequent analyses. Molecular weights and hydrodynamic radii were calculated from the MALS and DLS data, respectively, using the ASTRA 7 software (Wyatt). Additionally, Rg and I(0) values were obtained using the entire q-range of the data by calculating the distance distribution functions, P(r) vs. r, using GNOM (Svergun, 1992). All SEC-MALS-SAXS parameters for data collection and analysis can be found in Appendix Table S5.

Data availability

Expanded View for this article is available online.

Acknowledgements

Author contributions

Thuy P Dao: Conceptualization; investigation; methodology; writing – original draft; writing – review and editing. **Yiran Yang:** Investigation; methodology. **Maria F Presti:** Investigation. **Michael S Cosgrove:** Resources; investigation; writing – review and editing. **Jesse B Hopkins:** Resources; methodology. **Weikang Ma:** Resources; investigation. **Stewart N Loh:** Resources; methodology; writing – review and editing. **Carlos A Castañeda:** Conceptualization; resources; supervision; funding acquisition; methodology; writing – original draft; writing – review and editing.

In addition to the CRediT author contributions listed above, the contributions in detail are:

TPD and CAC involved in conceptualization; TPD, YY, JH, SNL, and CAC involved in methodology; TPD, YY, MSC, WM, and MFP involved in investigation; TPD and CAC involved in writing—original draft; TPD, MSC, SNL, and CAC involved in writing—review and editing; CAC involved in funding acquisition; CAC, MSC, JH, WM, and SNL involved in resources; CAC involved in supervision.

Disclosure and competing interest statement

The authors declare that they have no conflict interest.

References

Akutsu M, Dikic I, Bremm A (2016) Ubiquitin chain diversity at a glance. *J Cell Sci* 29: 875–880

Alexander EJ, Niaki AG, Zhang T, Sarkar J, Liu Y, Nirujogi RS, Pandey A, Myong S, Wang J (2018) Ubiquilin 2 modulates ALS/FTD-linked FUS–RNA complex dynamics and stress granule formation. *Proc Natl Acad Sci U S A* 115: E11485–E11494

Alshareedah I, Kaur T, Ngo J, Seppala H, Kounatse L-AD, Wang W, Moosa MM, Banerjee PR (2019) Interplay between short-range attraction and long-range repulsion controls reentrant liquid condensation of ribonucleoprotein–RNA complexes. *J Am Chem Soc* 141: 14593–14602

Banerjee PR, Milin AN, Moosa MM, Onuchic PL, Deniz AA (2017) Reentrant phase transition drives dynamic substructure formation in ribonucleoprotein droplets. *Angew Chem Int Ed Engl* 56: 11354–11359

Beal R, Deveraux Q, Xia G, Rechsteiner M, Pickart C (1996) Surface hydrophobic residues of multiubiquitin chains essential for proteolytic targeting. *Proc Natl Acad Sci U S A* 93: 861–866

Boughton AJ, Krueger S, Fushman D (2019) Branching via K11 and K48 bestows ubiquitin chains with a unique interdomain interface and enhanced affinity for proteasomal subunit Rpn1. *Structure* 28: 29–43.e6

Brautigam CA (2015) Calculations and publication-quality illustrations for analytical ultracentrifugation data. *Methods Enzymol* 562: 109–133

Brautigam CA, Padrick SB, Schuck P (2013) Multi-Signal Sedimentation Velocity Analysis with Mass Conservation for Determining the Stoichiometry of Protein Complexes. *PLoS One* 8: e62694

Bremm A, Freund SMV, Komander D (2010) Lys11-linked ubiquitin chains adopt compact conformations and are preferentially hydrolyzed by the deubiquitinase Cezanne. *Nat Struct Mol Biol* 17: 939–947

Buchan JR, Kolaitis R-M, Taylor JP, Parker R (2013) Eukaryotic stress granules are cleared by autophagy and Cdc48/VCP function. *Cell* 153: 1461–1474

Cabe M, Rademacher DJ, Karlsson AB, Cherukuri S, Bakowska JC (2018) PB1 and UBA domains of p62 are essential for aggresome-like induced structure formation. *Biochem Biophys Res Commun* 503: 2306–2311

Carvalho AF, Pinto MP, Grou CP, Vitorino R, Domingues P, Yamao F, Sá-Miranda C, Azevedo JE (2011) High-yield expression in *Escherichia coli* and

purification of mouse ubiquitin-activating enzyme E1. *Mol Biotechnol* 51: 254–261

Castañeda CA, Chaturvedi A, Camara CM, Curtis JE, Krueger S, Fushman D (2016) Linkage-specific conformational ensembles of non-canonical polyubiquitin chains. *Phys Chem Chem Phys* 18: 5771–5788

Castañeda CA, Dixon EK, Walker O, Chaturvedi A, Nakasone MA, Curtis JE, Reed MR, Krueger S, Cropp TA, Fushman D (2016) Linkage via K27 bestows ubiquitin chains with unique properties among polyubiquitins. *Structure* 24: 423–436

Ceballos-Diaz C, Rosario AM, Park H-J, Chakrabarty P, Sacino A, Cruz PE, Siemienski Z, Lara N, Moran C, Ravelo N *et al* (2015) Viral expression of ALS-linked ubiquilin-2 mutants causes inclusion pathology and behavioral deficits in mice. *Mol Neurodegener* 10: 25

Chen T, Huang B, Shi X, Gao L, Huang C (2018) Mutant UBQLN2P497H in motor neurons leads to ALS-like phenotypes and defective autophagy in rats. *Acta Neuropathol Commun* 6: 122

Choi J-M, Dar F, Pappu RV (2019) LASSI: A lattice model for simulating phase transitions of multivalent proteins. *PLoS Comput Biol* 15: e1007028

Dao TP, Castañeda CA (2020) Ubiquitin-modulated phase separation of shuttle proteins: does condensate formation promote protein degradation? *BioEssays* 42: e2000036

Dao TP, Kolaitis R-M, Kim HJ, O'Donovan K, Martyniak B, Colicino E, Hehnly H, Taylor JP, Castañeda CA (2018) Ubiquitin modulates liquid–liquid phase separation of UBQLN2 via disruption of multivalent interactions. *Mol Cell* 69: 965–978.e6

Dao TP, Martyniak B, Canning AJ, Lei Y, Colicino EG, Cosgrove MS, Hehnly H, Castañeda CA (2019) ALS-Linked Mutations Affect UBQLN2 Oligomerization and Phase Separation in a Position- and Amino Acid-Dependent Manner. *Structure* 27: 937–951.e5

Delaglio F, Grzesiek S, Vuister GW, Zhu G, Pfeifer J, Bax A (1995) NMRPIPE – a multidimensional spectral processing system based on UNIX pipes. *J Biomol NMR* 6: 277–293

Deng H-X, Chen W, Hong S-T, Boycott KM, Gorrie GH, Siddique N, Yang Y, Fecto F, Shi Y, Zhai H *et al* (2011) Mutations in UBQLN2 cause dominant X-linked juvenile and adult onset ALS and ALS/dementia. *Nature* 477: 211–215

Dignon GL, Best RB, Mittal J (2020) Biomolecular phase separation: from molecular driving forces to macroscopic properties. *Annu Rev Phys Chem* 71: 53–75

Dikic I (2017) Proteasomal and autophagic degradation systems. *Annu Rev Biochem* 86: 193–224

Eddins MJ, Varadan R, Fushman D, Pickart CM, Wolberger C (2007) Crystal structure and solution NMR studies of Lys48-linked tetraubiquitin at neutral pH. *J Mol Biol* 367: 204–211

Feric M, Demarest TG, Tian J, Croteau DL, Bohr VA, Misteli T (2021) Self-assembly of multi-component mitochondrial nucleoids via phase separation. *EMBO J* 40: e107165

Fu A, Cohen-Kaplan V, Avni N, Livneh I, Ciechanover A (2021) p62-containing, proteolytically active nuclear condensates, increase the efficiency of the ubiquitin–proteasome system. *Proc Natl Acad Sci U S A* 118: e2107321118

Gerson JE, Linton H, Xing J, Sutter AB, Kakos FS, Ryou J, Liggans N, Sharkey LM, Safren N, Paulson HL *et al* (2021) Shared and divergent phase separation and aggregation properties of brain-expressed ubiquilins. *Sci Rep* 11: 287

Guillén-Boixet J, Kopach A, Holehouse AS, Wittmann S, Jahnel M, Schlüßler R, Kim K, Trussina IREA, Wang J, Mateju D *et al* (2020) RNA-induced conformational switching and clustering of G3BP drive stress granule assembly by condensation. *Cell* 181: 346–361.e17

Gwon Y, Maxwell BA, Kolaitis R-M, Zhang P, Kim HJ, Taylor JP (2021) Ubiquitination of G3BP1 mediates stress granule disassembly in a context-specific manner. *Science* 372: eabf6548

Haglund K, Dikic I (2012) The role of ubiquitylation in receptor endocytosis and endosomal sorting. *J Cell Sci* 125: 265–275

Halloran M, Ragagnin AMG, Vidal M, Parakh S, Yang S, Heng B, Grima N, Shahheydari H, Soo K-Y, Blair I *et al* (2020) Amyotrophic lateral sclerosis-linked UBQLN2 mutants inhibit endoplasmic reticulum to Golgi transport, leading to Golgi fragmentation and ER stress. *Cell Mol Life Sci* 77: 3859–3873

Harman CA, Monteiro MJ (2019) The specificity of ubiquitin binding to ubiquilin-1 is regulated by sequences besides its UBA domain. *Biochim Biophys Acta Gen Subj* 1863: 1568–1574

Hipp MS, Park S-H, Hartl FU (2014) Proteostasis impairment in protein-misfolding and -aggregation diseases. *Trends Cell Biol* 24: 506–514

Hjerpe R, Bett JS, Keuss MJ, Solovyova A, McWilliams TG, Johnson C, Sahu I, Varghese J, Wood N, Wightman M *et al* (2016) UBQLN2 mediates autophagy-independent protein aggregate clearance by the proteasome. *Cell* 166: 935–949

Hoeller D, Hecker C-M, Wagner S, Rogov V, Dötsch V, Dikic I (2007) E3-independent monoubiquitination of ubiquitin-binding proteins. *Mol Cell* 26: 891–898

Hopkins JB, Gillilan RE, Skou S (2017) BioXTAS RAW: improvements to a free open-source program for small-angle X-ray scattering data reduction and analysis. *J Appl Crystallogr* 50: 1545–1553

Kaiser SE, Riley BE, Shaler TA, Trevino RS, Becker CH, Schulman H, Kopito RR (2011) Protein standard absolute quantification (PSAQ) method for the measurement of cellular ubiquitin pools. *Nat Methods* 8: 691–696

Kirby N, Cowieson N, Hawley AM, Mudie ST, McGillivray DJ, Kusel M, Samardzic-Boban V, Ryan TM (2016) Improved radiation dose efficiency in solution SAXS using a sheath flow sample environment. *Acta Crystallogr Sect Struct Biol* 72: 1254–1266

Komander D, Rape M (2012) The ubiquitin code. *Annu Rev Biochem* 81: 203–229

Labbadia J, Morimoto RI (2015) The biology of proteostasis in aging and disease. *Annu Rev Biochem* 84: 435–464

Laue TM, Shah BD, Ridgeway TM, Pelletier SL (1992) Computer-aided interpretation of analytical sedimentation data for proteins. In *Analytical ultracentrifugation in biochemistry and polymer science* pp 90–125. Cambridge: The Royal Society of Chemistry

Lin BC, Higgins NR, Phung TH, Monteiro MJ (2021) UBQLN proteins in health and disease with a focus on UBQLN2 in ALS/FTD. *FEBS J* https://doi.org/10.1111/febs.16129

Linares JF, Duran A, Yajima T, Pasparakis M, Moscat J, Diaz-Meco MT (2013) K63 polyubiquitination and activation of mTOR by the p62-TRAF6 complex in nutrient-activated cells. *Mol Cell* 51: 283–296

Long J, Gallagher TRA, Cavey JR, Sheppard PW, Ralston SH, Layfield R, Searle MS (2008) Ubiquitin recognition by the ubiquitin-associated domain of p62 involves a novel conformational switch. *J Biol Chem* 283: 5427–5440

Lowe J, Blanchard A, Morrell K, Lennox G, Reynolds L, Billett M, Landon M, Mayer RJ (1988) Ubiquitin is a common factor in intermediate filament inclusion bodies of diverse type in man, including those of Parkinson's disease, Pick's disease, and Alzheimer's disease, as well as Rosenthal fibres in cerebellar astrocytomas, cytoplasmic bodies in muscle, and mallory bodies in alcoholic liver disease. *J Pathol* 155: 9–15

Lu K, den Brave F, Jentsch S (2017) Receptor oligomerization guides pathway choice between proteasomal and autophagic degradation. *Nat Cell Biol* 19: 732–739

Maciejewski MW, Schuyler AD, Gryk MR, Moraru II, Romero PR, Ulrich EL, Eghbalnia HR, Livny M, Delaglio F, Hoch JC (2017) NMRbox: a resource for biomolecular NMR computation. *Biophys J* 112: 1529–1534

Manetto V, Perry G, Tabaton M, Mulvihill P, Fried VA, Smith HT, Gambetti P, Autilio-Gambetti L (1988) Ubiquitin is associated with abnormal cytoplasmic filaments characteristic of neurodegenerative diseases. *Proc Natl Acad Sci U S A* 85: 4501–4505

Molliex A, Temirov J, Lee J, Coughlin M, Kanagaraj AP, Kim HJ, Mittag T, Taylor JP (2015) Phase separation by low complexity domains promotes stress granule assembly and drives pathological fibrillization. *Cell* 163: 123–133

Morimoto D, Walinda E, Fukada H, Sou Y-S, Kageyama S, Hoshino M, Fujii T, Tsuchiya H, Saeki Y, Arita K *et al* (2015) The unexpected role of polyubiquitin chains in the formation of fibrillar aggregates. *Nat Commun* 6: 6116

Nathan JA, Tae Kim H, Ting L, Gygi SP, Goldberg AL (2013) Why do cellular proteins linked to K63-polyubiquitin chains not associate with proteasomes? *EMBO J* 32: 552–565

Nedelsky NB, Taylor JP (2019) Bridging biophysics and neurology: aberrant phase transitions in neurodegenerative disease. *Nat Rev Neurol* 15: 272–286

Olzmann JA, Li L, Chudaev MV, Chen J, Perez FA, Palmiter RD, Chin L-S (2007) Parkin-mediated K63-linked polyubiquitination targets misfolded DJ-1 to aggresomes via binding to HDAC6. *J Cell Biol* 178: 1025–1038

Padrick SB, Brautigam CA (2011) Evaluating the stoichiometry of macromolecular complexes using multisignal sedimentation velocity. *Methods* 54: 39–55

Park C-W, Ryu K-Y (2014) Cellular ubiquitin pool dynamics and homeostasis. *BMB Rep* 47: 475–482

Patel A, Lee HO, Jawerth L, Maharana S, Jahnel M, Hein MY, Stoynov S, Mahamid J, Saha S, Franzmann TM *et al* (2015) A liquid-to-solid phase transition of the ALS protein FUS accelerated by disease mutation. *Cell* 162: 1066–1077

Piper RC, Dikic I, Lukacs GL (2014) Ubiquitin-dependent sorting in endocytosis. *Cold Spring Harb Perspect Biol* 6: a016808

Raasi S, Varadan R, Fushman D, Pickart CM (2005) Diverse polyubiquitin interaction properties of ubiquitin-associated domains. *Nat Struct Mol Biol* 12: 708–714

Reber JM, Mangerich A (2021) Why structure and chain length matter: on the biological significance underlying the structural heterogeneity of poly (ADP-ribose). *Nucleic Acids Res* 49: 8432–8448

Riley BE, Kaiser SE, Shaler TA, Ng ACY, Hara T, Hipp MS, Lage K, Xavier RJ, Ryu K-Y, Taguchi K *et al* (2010) Ubiquitin accumulation in autophagy-deficient mice is dependent on the Nrf2-mediated stress response pathway: a potential role for protein aggregation in autophagic substrate selection. *J Cell Biol* 191: 537–552

Ruff KM, Dar F, Pappu RV (2021a) Ligand effects on phase separation of multivalent macromolecules. *Proc Natl Acad Sci U S A* 118, e2017184118

Ruff KM, Dar F, Pappu RV (2021b) Polyphasic linkage and the impact of ligand binding on the regulation of biomolecular condensates. *Biophys Rev* 2: 021302

Ryan VH, Fawzi NL (2019) Physiological, pathological, and targetable membraneless organelles in neurons. *Trends Neurosci* 42: 693–708

Sanders DW, Kedersha N, Lee DSW, Strom AR, Drake V, Riback JA, Bracha D, Eeftens JM, Iwanicki A, Wang A *et al* (2020) Competing protein-RNA interaction networks control multiphase intracellular organization. *Cell* 181: 306–324.e28

Schindelin J, Arganda-Carreras I, Frise E, Kaynig V, Longair M, Pietzsch T, Preibisch S, Rueden C, Saalfeld S, Schmid B *et al* (2012) Fiji: an open-source platform for biological-image analysis. *Nat Methods* 9: 676–682

Schuck P (2000) Size-distribution analysis of macromolecules by sedimentation velocity ultracentrifugation and lamm equation modeling. *Biophys J* 78: 619

Sharkey LM, Sandoval-Pistorius SS, Moore SJ, Gerson JE, Komlo R, Fischer S, Negron-Rios KY, Crowley EV, Padron F, Patel R *et al* (2020) Modeling UBQLN2-mediated neurodegenerative disease in mice: Shared and divergent properties of wild type and mutant UBQLN2 in phase separation, subcellular localization, altered proteostasis pathways, and selective cytotoxicity. *Neurobiol Dis* 143: 105016

Sontag EM, Samant RS, Frydman J (2017) Mechanisms and functions of spatial protein quality control. *Annu Rev Biochem* 86: 97−122

Sun D, Wu R, Zheng J, Li P, Yu L (2018) Polyubiquitin chain-induced p62 phase separation drives autophagic cargo segregation. *Cell Res* 28: 405−415

Svergun DI (1992) Determination of the regularization parameter in indirect-transform methods using perceptual criteria. *J Appl Crystallogr* 25: 495−503

Tenno T, Fujiwara K, Tochio H, Iwai K, Morita EH, Hayashi H, Murata S, Hiroaki H, Sato M, Tanaka K *et al* (2004) Structural basis for distinct roles of Lys63- and Lys48-linked polyubiquitin chains. *Genes Cells* 9: 865−875

Turco E, Witt M, Abert C, Bock-Bierbaum T, Su M-Y, Trapannone R, Sztacho M, Danieli A, Shi X, Zaffagnini G *et al* (2019) FIP200 claw domain binding to p62 promotes autophagosome formation at ubiquitin condensates. *Mol Cell* 74: 330−346.e11

Varadan R, Walker O, Pickart C, Fushman D (2002) Structural properties of polyubiquitin chains in solution. *J Mol Biol* 324: 637−647

Vendruscolo M (2012) Proteome folding and aggregation. *Curr Opin Struct Biol* 22: 138−143

Vranken WF, Boucher W, Stevens TJ, Fogh RH, Pajon A, Llinas M, Ulrich EL, Markley JL, Ionides J, Laue ED (2005) The CCPN data model for NMR spectroscopy: development of a software pipeline. *Proteins* 59: 687−696

Waudby CA, Christodoulou J (2020) NMR lineshape analysis of intrinsically disordered protein interactions. In *Intrinsically disordered proteins: methods and protocols*, BB Kragelund, K Skriver (eds) pp 477−504. New York, NY: Springer

Waudby CA, Ramos A, Cabrita LD, Christodoulou J (2016) Two-dimensional NMR lineshape analysis. *Sci Rep* 6: 24826

Williamson MP (2013) Using chemical shift perturbation to characterise ligand binding. *Prog Nucl Magn Reson Spectrosc* 73: 1−16

Wyman J, Gill SJ (1980) Ligand-linked phase changes in a biological system: applications to sickle cell hemoglobin. *Proc Natl Acad Sci U S A* 77: 5239−5242

Xu B, He G, Weiner BG, Ronceray P, Meir Y, Jonikas MC, Wingreen NS (2020) Rigidity enhances a magic-number effect in polymer phase separation. *Nat Commun* 11: 1561

Yang Y, Jones HB, Dao TP, Castañeda CA (2019) Single amino acid substitutions in stickers, but not spacers, substantially alter UBQLN2 phase transitions and dense phase material properties. *J Phys Chem B* 123: 3618−3629

Yang P, Mathieu C, Kolaitis R-M, Zhang P, Messing J, Yurtsever U, Yang Z, Wu J, Li Y, Pan Q *et al* (2020) G3BP1 Is a Tunable Switch that Triggers Phase Separation to Assemble Stress Granules. *Cell* 181: 325−345.e28

Yasuda S, Tsuchiya H, Kaiho A, Guo Q, Ikeuchi K, Endo A, Arai N, Ohtake F, Murata S, Inada T *et al* (2020) Stress- and ubiquitylation-dependent phase separation of the proteasome. *Nature* 578: 296−300

Ye Y, Blaser G, Horrocks MH, Ruedas-Rama MJ, Ibrahim S, Zhukov AA, Orte A, Klenerman D, Jackson SE, Komander D (2012) Ubiquitin chain conformation regulates recognition and activity of interacting proteins. *Nature* 492: 266−270

Zaffagnini G, Savova A, Danieli A, Romanov J, Tremel S, Ebner M, Peterbauer T, Sztacho M, Trapannone R, Tarafder AK *et al* (2018) p62 filaments capture and present ubiquitinated cargos for autophagy. *EMBO J* 37: e98308

Zhang Q, Huang H, Zhang L, Wu R, Chung C-I, Zhang S-Q, Torra J, Schepis A, Coughlin SR, Kornberg TB *et al* (2018) Visualizing dynamics of cell signaling *in vivo* with a phase separation-based kinase reporter. *Mol Cell* 69: 334−346.e4

Zhang D, Raasi S, Fushman D (2008) Affinity makes the difference: nonselective interaction of the UBA domain of ubiquilin-1 with monomeric ubiquitin and polyubiquitin chains. *J Mol Biol* 377: 162−180

Zheng T, Yang Y, Castañeda CA (2020) Structure, dynamics and functions of UBQLNs: at the crossroads of protein quality control machinery. *Biochem J* 477: 3471−3479

Zientara-Rytter K, Subramani S (2019) The Roles of Ubiquitin-Binding Protein Shuttles in the Degradative Fate of Ubiquitinated Proteins in the Ubiquitin-Proteasome System and Autophagy. *Cell* 8: 40